A Method to Compute the Probability of Positioning Failure for Vehicles in the Context of Dependence Between Parameter Estimation and Statistical Hypothesis Testing

Ciuban, Sebastian; Teunissen, Peter J.G.; Tiberius, Christian C.J.M.

DOI
10.1109/TVT.2025.3572368

Publication date
2025

Document Version
Final published version

Published in
IEEE Transactions on Vehicular Technology

Citation (APA)
Ciuban, S., Teunissen, P. J. G., & Tiberius, C. C. J. M. (2025). A Method to Compute the Probability of Positioning Failure for Vehicles in the Context of Dependence Between Parameter Estimation and Statistical Hypothesis Testing. *IEEE Transactions on Vehicular Technology*, *74*(10), 15238-15253. Article 3572368. https://doi.org/10.1109/TVT.2025.3572368

A Method to Compute the Probability of Positioning Failure for Vehicles in the Context of Dependence Between Parameter Estimation and Statistical Hypothesis Testing

Sebastian Ciuban, Peter J.G. Teunissen, *Senior Member, IEEE,* and Christian C.J.M. Tiberius

***Abstract*—Positioning technologies are widely used in automotive, aviation, rail, and maritime safety-critical applications. Therefore, the computation of the probability of positioning failure for vehicles, which is the probability that the position estimator is outside a safety region, is of interest for positioning safety analyses. Since parameter estimation and statistical hypothesis testing for model misspecifications are commonly employed in positioning algorithms, the resulting position estimator is conditioned on the statistical hypothesis testing outcome. Hence, the probability density function (PDF) of the vehicle position estimator that accounts for the dependence between the two inference concepts should be used in the computations. In this contribution, we propose a method to compute the probability of positioning failure using the PDF of the vehicle position estimator, which accounts for the aforementioned dependence and is based on rare event simulation techniques, specifically Importance Sampling and the Cross-Entropy method. We apply the proposed method to a satellite-based positioning scenario, in decimeter precision, of an automated vehicle. The results show that the proposed method enables extensive positioning safety-analyses giving insights that can be used in the development of positioning algorithms and deciding whether safety targets and/or requirements are met. Finally, we discuss some limitations of the method and propose several further improvements.**

***Index Terms*—Probability of positioning failure, Detection Identification and Adaptation (DIA), Rare event simulation, Importance Sampling, Cross-Entropy Method.**

I. Introduction

POSITIONING via Global Navigation Satellite Systems (GNSS) and/or Terrestrial Networked Positioning Systems (TNPS) is widely used and of interest, along with other sensors (inertial measurement units, cameras, LiDAR, etc.), in several safety-critical applications, such as automotive, aviation, rail, and maritime [1]–[5]. Based on these positioning technologies, a vehicle position estimator $\underline{\overline{x}} \in \mathbb{R}^n$ can be formulated and its probability density function (PDF) $f_{\underline{\overline{x}}}(x)$ can be obtained. Positioning safety analyses often have the objective to quantify the probability of the event of positioning failure $\mathcal{F} = \{\underline{\overline{x}} \in \mathcal{B}^c\}$ with $\mathcal{B}^c \subset \mathbb{R}^n$ being the complement of a chosen safety-region $\mathcal{B} \subset \mathbb{R}^n$ [6]. The *probability of positioning failure* is expressed as

$$\mathbb{P}_{\mathcal{F}} = \mathsf{P}\left(\underline{\overline{x}} \in \mathcal{B}^c\right) = \int_{\mathcal{B}^c} f_{\underline{\overline{x}}}(x)\, dx. \tag{1}$$

The authors are with the department of Geoscience and Remote Sensing, Delft University of Technology, 2628 CN Delft, The Netherlands (e-mail: ciuban.sebastian@gmail.com, p.j.g.teunissen@tudelft.nl, c.c.j.m.tiberius@tudelft.nl).

Based on (1), positioning safety analyses can be performed, and the obtained probability can be used to check compliance with application-specific requirements or guidelines (e.g., for automotive [7], or for aviation [6]). Moreover, there is a wide range of applications in which safety analyses are also based on the probability of failure, with respect to (w.r.t.) the events of interest, such as safety analyses for nuclear power plants, aerospace systems and structural safety [8]–[10].

The computation and analysis of (1) align with the scenario-based safety assessment framework used for automated and autonomous vehicles [11]–[13]. In accordance with the principles of this framework, positioning safety analyses can be conducted at the design stage of the positioning algorithms, where decisions are to be made regarding (i) measurement models, (ii) parameter estimation methods for the position vector, (iii) statistical hypothesis testing procedures to accommodate for model misspecifications (e.g., outliers or faults in measurements), and (iv) positioning scenarios for vehicles, among other factors. Since the vehicle's position estimator $\underline{\overline{x}} \in \mathbb{R}^n$ is often an outcome of parameter estimation and statistical hypothesis testing for model misspecifications [14]–[17], it is critical to account for the *dependence* between the two statistical inference concepts in the PDF $f_{\underline{\overline{x}}}(x)$. Teunissen has introduced a theoretical framework that rigorously treats this dependence and gives access to $f_{\underline{\overline{x}}}(x)$ in the distributional theory for the Detection, Identification, and Adaptation (DIA) method [18]. Failing to account for the dependence between parameter estimation and statistical hypothesis testing, the computation of (1) can lead to unrepresentative results (e.g., overly-optimistic [19], [20]). This type of implications has been recognized in various other disciplines such as mathematical statistics, biometrics, econometrics, and signal processing [21]–[26].

To perform positioning safety analyses, one must compute (1), which is challenging mainly because the PDF $f_{\underline{\overline{x}}}(x)$ is generally *multimodal* and its integration over the region $\mathcal{B}^c \subset \mathbb{R}^n$ for $n \geq 1$ is non-trivial. Existing methods in the GNSS positioning literature primarily focus on analytical upper-bounding techniques of $\mathbb{P}_{\mathcal{F}}$ based on univariate PDFs (i.e., when $n = 1$), which have been developed for civil aviation applications where the vertical component of the position estimator is of main interest [27]–[29]. Furthermore,

recent research explored upper-bounding approaches in the framework of Bayesian statistics and extreme value theory [30]–[32]. In the context of positioning safety for automotive applications, the extent to which the upper-bound overestimates its actual value when $n > 1$ (e.g., for a two-dimensional position vector) is still unclear or is not specifically addressed [33]–[35]. Therefore, we turn our attention to numerical integration techniques, such as Monte Carlo methods, to compute $\mathbb{P}_{\mathcal{F}}$ directly without upper-bounding it, which is a reasonable decision in the context of scenario-based safety assessments. However, if $\mathbb{P}_{\mathcal{F}}$ is required to be 'small' (e.g., $\mathbb{P}_{\mathcal{F}} < 10^{-7}$) then the standard Monte Carlo method becomes computationally inefficient due to the large pseudo-random samples needed to be generated from the PDF of interest $f_{\underline{\bar{x}}}(x)$ [36]. In this situation, one can apply principles from rare-event simulation [36], [37]. To the best of our knowledge, there is currently a lack of methods for computing (1) that address the challenges and shortcomings mentioned above, specifically accounting for the dependence between parameter estimation and statistical hypothesis testing. Therefore, we propose a method to compute (1) which: (i) exploits the structure of $f_{\underline{\bar{x}}}(x)$ by operating on its conditional components [18] while allowing the position vector to have a dimension $n \geq 1$, (ii) uses principles from rare-event simulation, specifically Importance Sampling (IS) and the Cross-Entropy (CE) method, for computing 'small' probabilities [37], [38], and (iii) quantifies the simulation uncertainty of the obtained results. We demonstrate the applicability of the method in the context of a GNSS-based decimeter precision level positioning scenario of an automated vehicle. The chosen scenario serves as an example and is not restricted to GNSS-based positioning as other positioning technologies can also be used (e.g., TNPS [2]). The methodological framework presented in this contribution is applicable beyond the automotive field, such as civil aviation, shipping, and rail. An extensive and component-wise positioning safety analysis is made possible for multivariate position estimators of vehicles while accounting for the dependence between parameter estimation and statistical hypothesis testing in their PDFs.

This contribution is organized as follows. In Section II we briefly review the main principles of the distributional theory for the DIA method to arrive at the expression of the estimator $\underline{\bar{x}} \in \mathbb{R}^n$ which captures the aforementioned dependence (called the DIA-estimator) and at the expression of its PDF $f_{\underline{\bar{x}}}(x)$. In the first part of Section III, we formulate the probability of positioning failure based on $f_{\underline{\bar{x}}}(x)$ and treat it as a rare event simulation problem. The second part of Section III describes the proposed method for the computation of (1) based on the principles of IS and the CE method. In Section IV we apply the proposed method to carry out a positioning safety analysis for an automated vehicle whose position vector is determined, at the decimeter level, based on GNSS. The probability of positioning failure is computed for a worst-case scenario, in a single epoch (snapshot) and as a function of the vehcile's orientation, based on which conclusions can be drawn whether safety targets or requirements are met. In Section IV we also discuss the limitations and potential improvements of the proposed method. Section V contains a summary and conclusions of this contribution while suggesting several directions for future work.

Throughout the paper we make use of the following notation: an underscore denotes a random quantity (e.g., the random vector $\underline{x} \in \mathbb{R}^n$), $f_{\underline{x}}(x)$ is the PDF of $\underline{x}$, $\mathsf{E}_{f_{\underline{x}}}(\underline{x})$ is the expectation operator, and $\mathsf{D}_{f_{\underline{x}}}(\underline{x})$ is the dispersion or variance operator. The joint PDF of two random vectors $\underline{x} \in \mathbb{R}^n$ and $\underline{t} \in \mathbb{R}^r$ is denoted $f_{\underline{x},\underline{t}}(x,t)$. The PDF of a random vector $\underline{x}$ conditioned on an event $\mathcal{E}$ is denoted $f_{\underline{x}|\mathcal{E}}(x|\mathcal{E})$. The probability of an event $\mathcal{E}$ is denoted by $\mathsf{P}_{\mathcal{E}} = \mathsf{P}(\mathcal{E})$. A projection matrix is denoted as $\mathbf{\Pi}_{\mathrm{A}}$ and it projects orthogonally (w.r.t. some metric) onto the range space of the matrix $\mathrm{A} \in \mathbb{R}^{m \times n}$ ($\mathcal{R}(\mathrm{A})$). For the weighted squared norm of a vector, we use the notation $||.||^2_{\mathrm{Q}} = (.)^T\mathrm{Q}^{-1}(.)$. If the squared norm is w.r.t. the identity matrix then it is denoted $||.||^2$.

II. Review of Combined Parameter Estimation and Statistical Hypothesis Testing

In this section we review the main principles of the distributional theory for the Detection, Identification, and Adaptation (DIA) method [18]. Based on these principles, the PDF of the DIA-estimator, which accounts for the statistical dependence between parameter estimation and statistical hypothesis testing, is obtained. This PDF is then used to formulate the probability of positioning failure in Section III.

Let us assume a random vector of observables (e.g., based on the (pseudo)range measurements from a positioning system) $\underline{y} \in \mathbb{R}^m$ which is normally distributed

$$\underline{y} \sim \mathcal{N}(\mathrm{Ax}, \mathrm{Q}_{\mathrm{yy}}), \tag{2}$$

where $\mathrm{A} \in \mathbb{R}^{m \times n}$ is the design matrix with $\mathrm{rank}(\mathrm{A}) = n$, $\mathrm{x} \in \mathbb{R}^n$ is the vector of unknown parameters, and $\mathrm{Q}_{\mathrm{yy}} \in \mathbb{R}^{m \times m}$ is the symmetric positive definite variance-covariance matrix of $\underline{y} \in \mathbb{R}^m$. We consider model misspecifications of the mean of $\underline{y}$ (e.g., due to outliers in the observables) as these are the most common in practice [39]. The following multiple statistical hypothesis testing problem is formulated,

$$\mathcal{H}_0 : \mathsf{E}_{f_{\underline{y}}}(\underline{y}) = \mathrm{Ax} \quad \text{vs.} \quad \mathcal{H}_{i\neq 0} : \mathsf{E}_{f_{\underline{y}}}(\underline{y}) = \mathrm{Ax} + \mathrm{C}_i\mathrm{b}_i \tag{3}$$

for $i \in \{0, ..., k\}$, where $\mathrm{C}_i \in \mathbb{R}^{m \times q_i}$ models the type of model misspecification, $\mathrm{rank}([\mathrm{A}, \mathrm{C}_i]) = n + q_i$, and $\mathrm{b}_i \in \mathbb{R}^{q_i}$ is the model misspecification (e.g., outlier). The redundancy of $\mathcal{H}_0$ is $r = m - \mathrm{rank}(\mathrm{A})$. The statistical testing procedure can be designed using the vector of misclosures

$$\underline{t} = \mathrm{B}^T\underline{y}, \quad \mathrm{Q}_{\mathrm{tt}} = \mathrm{B}^T\mathrm{Q}_{\mathrm{yy}}\mathrm{B}, \tag{4}$$

where $\mathrm{B} \in \mathbb{R}^{m \times r}$ is a basis matrix of $\mathcal{R}(\mathrm{A})^{\perp}$ (i.e., $\mathrm{B}^T\mathrm{A} = 0_{r \times n}$). The vector of misclosures provides a measure of inconsistency between the model under $\mathcal{H}_0$ and the observations, and has its dimension equal to the redundancy r. Furthermore, it is possible to link the Best Linear Unbiased Estimators

(BLUEs) of $\mathrm{x} \in \mathbb{R}^n$ under the $\mathcal{H}_{i\neq 0}$'s and $\mathcal{H}_0$ using $\underline{\mathrm{t}} \in \mathbb{R}^r$ as follows [18]

$$\begin{bmatrix} \underline{\hat{\mathrm{x}}}_i \\ \underline{\mathrm{t}} \end{bmatrix} = \underbrace{\begin{bmatrix} \mathrm{I}_n & -\mathrm{L}_i \\ 0_{r\times n} & \mathrm{I}_r \end{bmatrix}}_{\mathrm{V}_i} \begin{bmatrix} \underline{\hat{\mathrm{x}}}_0 \\ \underline{\mathrm{t}} \end{bmatrix}, \text{ with } \mathrm{L}_i = \begin{cases} 0_{n\times r} & , i = 0 \\ \mathrm{A}^+\mathrm{C}_i\mathrm{C}_{\mathrm{t}_i}^+ & , i > 0 \end{cases} \tag{5}$$

where $\underline{\hat{\mathrm{x}}}_0 = \mathrm{A}^+\underline{\mathrm{y}}$ and $\mathrm{A}^+ = (\mathrm{A}^T\mathrm{Q}_{\mathrm{yy}}^{-1}\mathrm{A})^{-1}\mathrm{A}^T\mathrm{Q}_{\mathrm{yy}}^{-1}$ from the system of normal equations $(\mathrm{A}^T\mathrm{Q}_{\mathrm{yy}}^{-1}\mathrm{A})\,\underline{\hat{\mathrm{x}}}_0 = \mathrm{A}^T\mathrm{Q}_{\mathrm{yy}}^{-1}\underline{\mathrm{y}}$. The BLUE-inverse of $\mathrm{C}_{\mathrm{t}_i} = \mathrm{B}^T\mathrm{C}_i$ is $\mathrm{C}_{\mathrm{t}_i}^+ = (\mathrm{C}_{\mathrm{t}_i}^T\mathrm{Q}_{\mathrm{tt}}^{-1}\mathrm{C}_{\mathrm{t}_i})^{-1}\mathrm{C}_{\mathrm{t}_i}^T\mathrm{Q}_{\mathrm{tt}}^{-1}$. Note that the transformation in (5) is in block-triangular form and its inverse is simply $\mathrm{V}_i^{-1} = \begin{bmatrix} \mathrm{I}_n & \mathrm{L}_i \\ 0_{r\times n} & \mathrm{I}_r \end{bmatrix}$. The PDF of $\begin{bmatrix} \underline{\hat{\mathrm{x}}}_i^T & \underline{\mathrm{t}}^T \end{bmatrix}^T$, under a $\mathcal{H}_a$, is

$$\mathcal{H}_a : \begin{bmatrix} \underline{\hat{\mathrm{x}}}_i \\ \underline{\mathrm{t}} \end{bmatrix} \sim \mathcal{N}\left(\begin{bmatrix} \mathrm{x} + \mathrm{A}^+\mathrm{R}_i\mathrm{C}_a\mathrm{b}_a \\ \mathrm{B}^T\mathrm{C}_a\mathrm{b}_a \end{bmatrix}, \begin{bmatrix} \mathrm{Q}_{\hat{\mathrm{x}}_0\hat{\mathrm{x}}_0} + \mathrm{L}_i\mathrm{Q}_{\mathrm{tt}}\mathrm{L}_i^T & -\mathrm{L}_i\mathrm{Q}_{\mathrm{tt}} \\ -\mathrm{Q}_{\mathrm{tt}}\mathrm{L}_i^T & \mathrm{Q}_{\mathrm{tt}} \end{bmatrix} \right), \tag{6}$$

where $\mathrm{R}_i = \mathrm{I}_m - \mathrm{C}_i\left(\mathrm{B}^T\mathrm{C}_i\right)^+\mathrm{B}^T$ projects along $\mathcal{R}(\mathrm{C}_i)$ and onto $\mathcal{R}(\mathrm{A}, \mathrm{Q}_{\mathrm{yy}}\mathrm{B}(\mathrm{B}^T\mathrm{C}_i)^\perp)$ with $(\mathrm{B}^T\mathrm{C}_i)^\perp$ being a basis matrix of the null space of $\mathrm{C}_i^T\mathrm{B}$. The variance-covariance $\mathrm{Q}_{\hat{\mathrm{x}}_0\hat{\mathrm{x}}_0} = (\mathrm{A}^T\mathrm{Q}_{\mathrm{yy}}^{-1}\mathrm{A})^{-1}$ is the one of $\underline{\hat{\mathrm{x}}}_0$. For a given $\mathcal{H}_a$, we emphasize the following two-cases for the joint PDF of $\begin{bmatrix} \underline{\hat{\mathrm{x}}}_i^T & \underline{\mathrm{t}}^T \end{bmatrix}^T$,

$$f_{\underline{\hat{\mathrm{x}}}_i,\underline{\mathrm{t}}}(x,t) \begin{cases} = f_{\underline{\hat{\mathrm{x}}}_0}(x) f_{\underline{\mathrm{t}}}(t) & , \text{ if } i = 0 \\ \neq f_{\underline{\hat{\mathrm{x}}}_i}(x) f_{\underline{\mathrm{t}}}(t) & , \text{ if } i > 0, \end{cases} \tag{7}$$

which shows that, for $i > 0$, the BLUEs $\underline{\hat{\mathrm{x}}}_i$ and the misclosure vector $\underline{\mathrm{t}}$ are *dependent*.

A. Partitioning of misclosure vector space

Partitioning principles are applied to the misclosure vector space $\mathbb{R}^r$ to 'map' the hypothesis testing problem (3) to a partitioning problem. A partition of $\mathbb{R}^r$ can be formulated based on $\mathcal{P}_i \subset \mathbb{R}^r$, for $i \in \{0, ..., k\}$ such that $\cup_{i=0}^k \mathcal{P}_i = \mathbb{R}^r$ and $\mathcal{P}_i \cap \mathcal{P}_l = \{0\}$ for $i \neq l$. Hypothesis $\mathcal{H}_i$, for $i \in \{0, ..., k\}$, is selected as the most likely one if and only if $\underline{\mathrm{t}} \in \mathcal{P}_i$, leading to the result of the procedure: $\underline{\hat{\mathrm{x}}}_i$. The partitions can be defined as follows

$$\begin{aligned} \mathcal{P}_0 &= \left\{ t \in \mathbb{R}^r \mid ||t||_{\mathrm{Q}_{\mathrm{tt}}}^2 \leq \chi_\alpha^2(r,0) \right\}, \\ \mathcal{P}_{i\neq 0} &= \left\{ t \in \mathbb{R}^r \mid t \notin \mathcal{P}_0,\ \check{\mathrm{T}}_i = \max_{l\in\{1,...,k\}} \mathrm{T}_l \right\}, \end{aligned} \tag{8}$$

where $||\underline{\mathrm{t}}||_{\mathrm{Q}_{\mathrm{tt}}}^2$ is the overall model test statistic, $\chi_\alpha^2(r,0)$ is the critical value for a level of significance α, and $\underline{\mathrm{T}}_l$ is the result of the following transformation [39], [40]

$$\underline{\mathrm{T}}_l = \mathrm{CDF}_{\chi^2(q_l,0)}\left(||\mathbf{\Pi}_{\mathrm{C}_{\mathrm{t}_l}}\underline{\mathrm{t}}||_{\mathrm{Q}_{\mathrm{tt}}}^2 \right), \tag{9}$$

where $\mathrm{CDF}_{\chi^2(q_l,0)}(.)$ is the cumulative distribution function (CDF) of $\chi^2(q_l,0)$, $||\mathbf{\Pi}_{\mathrm{C}_{\mathrm{t}_l}}\underline{\mathrm{t}}||_{\mathrm{Q}_{\mathrm{tt}}}^2 \overset{\mathcal{H}_0}{\sim} \chi^2(q_l,0)$, $\mathbf{\Pi}_{\mathrm{C}_{\mathrm{t}_l}} = \mathrm{C}_{\mathrm{t}_l}\mathrm{C}_{\mathrm{t}_l}^+$, and $\underline{\mathrm{T}}_l$ has a uniform distribution on the interval $[0,1]$ under $\mathcal{H}_0$. In this way, all $\underline{\mathrm{T}}_l$'s will have the same PDF under $\mathcal{H}_0$, since the dimension of the model misspecification $\mathrm{b}_l \in \mathbb{R}^{q_l}$ would generally differ across the alternative hypotheses. Therefore, the maximum among them ($\check{\underline{\mathrm{T}}}_i$) corresponds to the most likely $\mathcal{H}_{i\neq 0}$. Note that if the dimension of the model misspecification is the same across the alternative hypotheses, then the transformation step in (9) is not needed and the maximum across $||\mathbf{\Pi}_{\mathrm{C}_{\mathrm{t}_l}}\underline{\mathrm{t}}||_{\mathrm{Q}_{\mathrm{tt}}}^2$ can be found directly to obtain $\check{\underline{\mathrm{T}}}_i$. Fig. 1(a) shows partitions obtained for a simple example. For other types of partitions (e.g., inclusion of undecided regions when discriminating between hypotheses is challenging), we refer to [41]. We also mention that the statistical hypothesis testing procedure can be formulated equally, based on the residual vector $\underline{\hat{\mathrm{e}}}_0 = \underline{\mathrm{y}} - \mathrm{A}\underline{\hat{\mathrm{x}}}_0$, which gives $\underline{\hat{\mathrm{e}}}_0 = \mathrm{Q}_{\mathrm{yy}}\mathrm{B}\,\mathrm{Q}_{\mathrm{tt}}^{-1}\underline{\mathrm{t}}$ leading to the equality of the quadratic forms $||\underline{\hat{\mathrm{e}}}_0||_{\mathrm{Q}_{\mathrm{yy}}}^2 = ||\underline{\mathrm{t}}||_{\mathrm{Q}_{\mathrm{tt}}}^2 \overset{\mathcal{H}_0}{\sim} \chi^2(r,0)$.

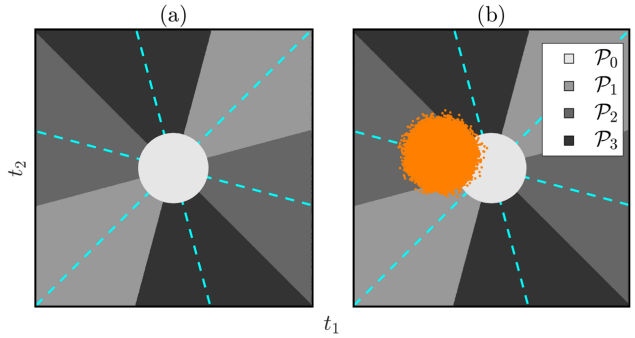

Fig. 1. (a) Partition of $\mathbb{R}^{r=2}$ when $\mathrm{A} = [1\ 1\ 1]^T$, $\mathrm{x} \in \mathbb{R}$, $\mathrm{Q}_{\mathrm{yy}} = \mathrm{I}_3$, and $\mathrm{C}_i = \mathrm{c}_i$'s are the canonical unit vectors for $i = \{1, 2, 3\}$. The dashed lines (in cyan) are the spans of the vectors $\mathrm{B}^T\mathrm{c}_i$. (b) Partition of $\mathbb{R}^{r=2}$ along with pseudo-random samples ('dots' coloured in orange) generated from $f_{\underline{\mathrm{t}}}(t|\mathcal{H}_2)$ (as an example). Under $\mathcal{H}_2$, the samples from $f_{\underline{\mathrm{t}}}(t|\mathcal{H}_2)$ are shifted away from the origin along the vector span of $\mathrm{B}^T\mathrm{c}_2$.

B. Statistical hypothesis testing decisions and their probabilities

The decision outcome in statistical hypothesis testing is determined by where the misclosure vector $\underline{\mathrm{t}}$ lands in $\mathbb{R}^r$ with partitions $\mathcal{P}_i \subset \mathbb{R}^r$, for $i \in \{0, .., k\}$. Under $\mathcal{H}_0$, the decision results are: (i) Correct Acceptance (CA) of $\mathcal{H}_0$ when $\underline{\mathrm{t}} \in \mathcal{P}_0$, and (ii) False Alarm (FA) when $\underline{\mathrm{t}} \notin \mathcal{P}_0$, or specifically the FA per alternative hypothesis when $\underline{\mathrm{t}} \in \mathcal{P}_i$ for $i > 0$. The probabilities of these decisions are given by

$$\mathrm{P}_{\mathrm{CA}} = \mathrm{P}\left(\underline{\mathrm{t}} \in \mathcal{P}_0 | \mathcal{H}_0\right), \quad \mathrm{P}_{\mathrm{FA}} = \sum_{i=1}^k \mathrm{P}\left(\underline{\mathrm{t}} \in \mathcal{P}_i | \mathcal{H}_0\right), \tag{10}$$

where $\mathrm{P}\left(\underline{\mathrm{t}} \in \mathcal{P}_i | \mathcal{H}_0\right) = \mathrm{P}_{\mathrm{FA}_i}$, $\mathrm{P}_{\mathrm{FA}} = \sum_{i=1}^k \mathrm{P}_{\mathrm{FA}_i} = \alpha$ is the level of significance, and $\mathrm{P}_{\mathrm{CA}} + \mathrm{P}_{\mathrm{FA}} = 1$. Similarly, under $\mathcal{H}_a$, for $a > 0$, the outcomes of the decisions are: (i) missed detection (MD) when $\underline{\mathrm{t}} \in \mathcal{P}_0$, (ii) Correct Identification (CI) when $\underline{\mathrm{t}} \in \mathcal{P}_a$, and (iii) Wrong Identification (WI) $\underline{\mathrm{t}} \in \mathcal{P}_i$ for $i \notin \{0, a\}$ (see Fig. 1(b)). The probabilities of these decisions are given by

$$\begin{aligned} \mathrm{P}_{\mathrm{MD}_a} &= \mathrm{P}\left(\underline{\mathrm{t}} \in \mathcal{P}_0 | \mathcal{H}_a\right), \quad \mathrm{P}_{\mathrm{CI}_a} = \mathrm{P}\left(\underline{\mathrm{t}} \in \mathcal{P}_a | \mathcal{H}_a\right), \\ \mathrm{P}_{\mathrm{WI}} &= \sum_{i\neq 0,a}^k \mathrm{P}\left(\underline{\mathrm{t}} \in \mathcal{P}_i | \mathcal{H}_a\right), \end{aligned} \tag{11}$$

where $\mathsf{P}\left(\underline{\mathrm{t}} \in \mathcal{P}_i|\mathcal{H}_a\right) = \mathsf{P}_{\mathrm{WI}_i}$ and the decision outcome of Correct Detection (CD) is given by $\mathsf{P}_{\mathrm{CD}_a} = \mathsf{P}_{\mathrm{CI}_a} + \mathsf{P}_{\mathrm{WI}}$ fulfilling $\mathsf{P}_{\mathrm{MD}_a} + \mathsf{P}_{\mathrm{CD}_a} = 1$. The probabilities in (11) depend on the unknown model misspecification $\mathrm{b}_a \in \mathbb{R}^{q_a}$ since $f_{\underline{\mathrm{t}}}(t|\mathcal{H}_a) = \mathcal{N}\left(\mathrm{B}^T\mathrm{C}_a\mathrm{b}_a, \mathrm{Q}_{\mathrm{tt}}\right)$.

C. DIA-estimator and its PDF

The *combined* parameter estimation and statistical hypothesis testing procedure, in the forms discussed previously, can be captured by the Detection (D) Identification (I) and Adaptation (A) procedure, summarized as follows

$$\begin{cases} \text{if } \underline{\mathrm{t}} \in \mathcal{P}_0 \text{ (no D)} \rightarrow \text{ output } \hat{\underline{\mathrm{x}}}_0, \\ \text{if } \underline{\mathrm{t}} \notin \mathcal{P}_0 \text{ (D)} \rightarrow \underline{\mathrm{t}} \in \mathcal{P}_{i\neq 0} \text{ (I)} \rightarrow \text{ output } \hat{\underline{\mathrm{x}}}_i \text{ (A)}. \end{cases} \tag{12}$$

The procedure in (12), or any procedure of similar form (e.g., [27]), can expressed in terms of the DIA-estimator

$$\overline{\underline{\mathrm{x}}} = \begin{cases} \hat{\underline{\mathrm{x}}}_0, & \text{if } \underline{\mathrm{t}} \in \mathcal{P}_0 \\ \hat{\underline{\mathrm{x}}}_i, & \text{if } \underline{\mathrm{t}} \in \mathcal{P}_{i\neq 0} \end{cases} \xrightarrow{\text{compact form}} \quad \overline{\underline{\mathrm{x}}} = \sum_{i=0}^{k} \hat{\underline{\mathrm{x}}}_i \, p_i(\underline{\mathrm{t}}) \ , \tag{13}$$

where the indicator function $p_i(\underline{\mathrm{t}}) = 1$ if $\underline{\mathrm{t}} \in \mathcal{P}_i$ and 0 otherwise. The PDF of $\overline{\underline{\mathrm{x}}}$ follows from Theorem 1 in [18]

$$f_{\overline{\underline{\mathrm{x}}}}(x) = \sum_{i=0}^{k} \int_{\mathcal{P}_i} f_{\hat{\underline{\mathrm{x}}}_i, \underline{\mathrm{t}}}(x, t)\, dt, \tag{14}$$

which, in general, is a multimodal PDF. The conditional components of $f_{\overline{\underline{\mathrm{x}}}}(x)$ on the testing decisions of CA, FA_i, MD_a, CI_a, and WI_i can be obtained from $f_{\overline{\underline{\mathrm{x}}}}(x|\mathcal{H}_0)$ and $f_{\overline{\underline{\mathrm{x}}}}(x|\mathcal{H}_a)$ for $a \neq 0$. The probability of positioning failure and its conditional components are formulated in Section III, based on (14), together with the proposed method to compute them.

D. Remarks on the dimensions of vector spaces

In this subsection we make several remarks about the dimensionality of the unknown parameter $\mathrm{x} \in \mathbb{R}^n$ and of the misclosure vector $\underline{\mathrm{t}} \in \mathbb{R}^r$ for GNSS-based positioning applications. One may not be interested in the complete parameter vector $\mathrm{x} \in \mathbb{R}^n$, but only in the components corresponding to the 1D, 2D, or 3D position. The linear transformation that gives the desired position components can be expressed as $\theta = \mathrm{H}^T\mathrm{x} \in \mathbb{R}^p$ with $p < n$. Further developments are done in terms of $\mathrm{x} \in \mathbb{R}^n$, however a similar route would apply also for $\theta \in \mathbb{R}^p$ [18].

The redundancy under $\mathcal{H}_0$, and therefore the dimension of the misclosure vector $\underline{\mathrm{t}} \in \mathbb{R}^r$, depends on the chosen positioning technology, like, for example, GNSS. In this case it depends on the number of observed GNSS satellites, type of observables, from how many frequencies these observables are obtained, the number of parameters to be estimated, etc [42]. As we will see in Section IV, in the case of a GNSS receiver which obtains code-based pseudoranges from 15 GNSS satellites of two constellations (e.g., 8 GPS and 7 Galileo satellites) at a single-epoch (snapshot), on a single-frequency, with the objective to estimate the 3D position vector and the receiver clock bias, then (i) $r = 15 - 4 - 1 = 10$ if the Inter System Bias (ISB) is considered unknown, or (ii) $r = 15 - 4 = 11$ if the ISB is considered known [42]. If more than two GNSS constellations are considered, under similar assumptions, r could reach values around 40.

III. Method to compute the probability of positioning failure and its components

In this section we present the expression of the probability of positioning failure, its conditional components, and introduce a method developed to compute them. The starting point is the probability of positioning failure re-expressed from (1)

$$\mathbb{P}_{\mathcal{F}}(\mathbf{b}) = \int_{\mathcal{B}^c} f_{\overline{\underline{\mathrm{x}}}}(x)\, dx, \tag{15}$$

where the dependence on the model misspecifications is accounted in the notation with $\mathbf{b} = \{\mathrm{b}_1, ..., \mathrm{b}_k\}$ for $i > 0$, and $\mathcal{B}^c = \mathbb{R}^n/\mathcal{B}$ is the complement of the safety-region $\mathcal{B} \subset \mathbb{R}^n$. Applying the law of total probability to (15) yields

$$\begin{aligned} \mathbb{P}_{\mathcal{F}}(\mathbf{b}) = \mathsf{P}(\mathcal{H}_0) \underbrace{\left(\int_{\mathcal{B}^c} f_{\overline{\underline{\mathrm{x}}}}(x|\mathcal{H}_0)\, dx \right)}_{\mathbb{P}_{\mathcal{F}}|\mathcal{H}_0} + \\ \sum_{i=1}^{k} \mathsf{P}(\mathcal{H}_i) \underbrace{\left(\int_{\mathcal{B}^c} f_{\overline{\underline{\mathrm{x}}}}(x|\mathcal{H}_i)\, dx \right)}_{\mathbb{P}_{\mathcal{F}}|\mathcal{H}_i(\mathrm{b}_i)}, \end{aligned} \tag{16}$$

with $\mathsf{P}(\mathcal{H}_0)$ and $\mathsf{P}(\mathcal{H}_i)$, for $i > 0$, denote the apriori probabilities of the hypotheses. Combining (14) and (16), it follows that

$$\begin{aligned} \mathbb{P}_{\mathcal{F}}(\mathbf{b}) = \mathsf{P}(\mathcal{H}_0) \left(\sum_{j=0}^{k} \mathsf{E}_{f_{\hat{\underline{\mathrm{x}}}_j, \underline{\mathrm{t}}}} \left(\mathbb{1}_j(\underline{\mathrm{x}}, \underline{\mathrm{t}}) | \mathcal{H}_0 \right) \right) + \\ \sum_{i=1}^{k} \mathsf{P}(\mathcal{H}_i) \left(\sum_{j=0}^{k} \mathsf{E}_{f_{\hat{\underline{\mathrm{x}}}_j, \underline{\mathrm{t}}}} \left(\mathbb{1}_j(\underline{\mathrm{x}}, \underline{\mathrm{t}}) | \mathcal{H}_i \right) \right), \end{aligned} \tag{17}$$

where the 'joint' indicator function $\mathbb{1}_j(\underline{\mathrm{x}}, \underline{\mathrm{t}}) = 1$ if $[\underline{\mathrm{x}}^T \ \underline{\mathrm{t}}^T]^T \in (\mathcal{B}^c \cap \mathcal{P}_j)$, and 0 otherwise. The two summations of joint probabilities in parentheses in (17) are rewritten below, explicitly incorporating the statistical testing decisions into the notation,

$$\begin{aligned} \sum_{j=0}^{k} \mathsf{E}_{f_{\hat{\underline{\mathrm{x}}}_j, \underline{\mathrm{t}}}} \left(\mathbb{1}_j(\underline{\mathrm{x}}, \underline{\mathrm{t}}) | \mathcal{H}_0 \right) = \mathbb{P}_{\mathcal{F}}|\mathrm{CA}\, \mathsf{P}_{\mathrm{CA}} + \sum_{j=1}^{k} \mathbb{P}_{\mathcal{F}}|\mathrm{FA}_j\, \mathsf{P}_{\mathrm{FA}_j}, \\ \sum_{j=0}^{k} \mathsf{E}_{f_{\hat{\underline{\mathrm{x}}}_j, \underline{\mathrm{t}}}} \left(\mathbb{1}_j(\underline{\mathrm{x}}, \underline{\mathrm{t}}) | \mathcal{H}_i \right) = \mathbb{P}_{\mathcal{F}}|\mathrm{MD}_i\, \mathsf{P}_{\mathrm{MD}_i} + \mathbb{P}_{\mathcal{F}}|\mathrm{CI}_i\, \mathsf{P}_{\mathrm{CI}_i} + \\ \sum_{j\neq 0,i}^{k} \mathbb{P}_{\mathcal{F}}|\mathrm{WI}_j\, \mathsf{P}_{\mathrm{WI}_j} \ . \end{aligned} \tag{18}$$

where $\mathbb{P}_{\mathcal{F}}|\mathcal{E}$ is the probability of positioning failure conditioned on the testing decision $\mathcal{E} \in \{\mathrm{CA}, \mathrm{FA}_j, \mathrm{MD}_i, \mathrm{CI}_i, \mathrm{WI}_j\}$. These decompositions are schematically illustrated as a 'failure-tree' in Fig. 2, where Level 1 corresponds to (18) and Level 2 corresponds to (16).

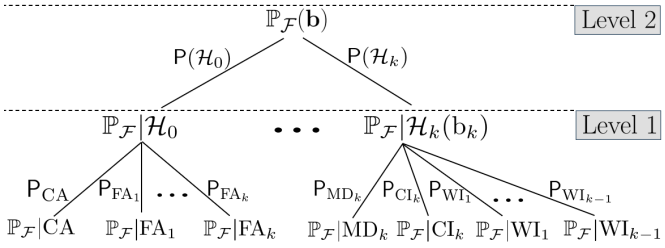

Fig. 2. Representation of $\mathbb{P}_{\mathcal{F}}(\mathbf{b})$ as a 'failure-tree'. Level 1 corresponds to (18) and Level 2 to (16).

The objective of our proposed method is to construct the 'failure-tree' in Fig. 2 by computing all of the components from Levels 1 and 2.

A. Computation of Level 1 Components

To illustrate the computational steps for an arbitrary component from Level 1, we introduce the following generic notation

$$\mathbb{P}_{\mathcal{F}}|\mathcal{H} = \begin{cases} \mathbb{P}_{\mathcal{F}}|\mathcal{H}_0, & \text{if } \mathcal{H} = \mathcal{H}_0 \\ \mathbb{P}_{\mathcal{F}}|\mathcal{H}_i(\mathrm{b}_i), & \text{if } \mathcal{H} = \mathcal{H}_i \text{ for } i \in \{1, ..., k\} \end{cases}. \tag{19}$$

From (17) it follows that

$$\mathbb{P}_{\mathcal{F}}|\mathcal{H} = \sum_{j=0}^{k} \underbrace{\mathsf{E}_{f_{\underline{\hat{\mathrm{x}}}_j, \underline{\mathrm{t}}}}\left(\mathbb{1}_j(\underline{\mathrm{x}}, \underline{\mathrm{t}})|\mathcal{H}\right)}_{\mathcal{X}_j}, \tag{20}$$

where $\mathcal{X}_j$ denotes the j^{th} joint-probability component of the sum. The first step is to reparametrize the components $\mathcal{X}_j$, noting that the number of distributional parameters defining each $f_{\underline{\hat{\mathrm{x}}}_j, \underline{\mathrm{t}}}(x, t|\mathcal{H})$ increases quadratically, up to $[(n+r) + (n+r)(n+r+1)/2]$, primarily due to the variance-covariance matrix. To mitigate this quadratic increase in dimensionality we start from

$$\underline{\mathrm{s}}_j = \begin{bmatrix} \underline{\hat{\mathrm{x}}}_j \\ \underline{\mathrm{t}} \end{bmatrix}, \quad \mathrm{Q}_{\mathrm{s}_j\mathrm{s}_j} = \begin{bmatrix} \mathrm{Q}_{\hat{\mathrm{x}}_0\hat{\mathrm{x}}_0} + \mathrm{L}_j\mathrm{Q}_{\mathrm{tt}}\mathrm{L}_j^T & -\mathrm{L}_j\mathrm{Q}_{\mathrm{tt}} \\ -\mathrm{Q}_{\mathrm{tt}}\mathrm{L}_j^T & \mathrm{Q}_{\mathrm{tt}} \end{bmatrix}. \tag{21}$$

An approach is to apply a change of variable to the expected values in (20) such that they are expressed w.r.t. PDFs which have simpler forms (e.g., identity variance-covariance matrices) [43]. Suppose an invertible linear transformation defined by $\mathrm{U}_j : \mathbb{R}^{(n+r)} \to \mathbb{R}^{(n+r)}$ applied to (21), which gives the following pair

$$\underline{\mathrm{z}}_j = \mathrm{U}_j\,\underline{\mathrm{s}}_j, \qquad \underline{\mathrm{s}}_j = \mathrm{U}_j^{-1}\underline{\mathrm{z}}_j\ . \tag{22}$$

One could make use of the *readily-available* transformation in the block-triangular form V_j in (5) and its inverse to set

$$\mathrm{U}_j = \begin{bmatrix} \mathrm{I}_n & \mathrm{L}_j \\ 0_{r\times n} & \mathrm{I}_r \end{bmatrix} \to \mathrm{Q}_{\mathrm{z}_j\mathrm{z}_j} = \begin{bmatrix} \mathrm{Q}_{\hat{\mathrm{x}}_0\hat{\mathrm{x}}_0} & 0_{n\times r} \\ 0_{r\times n} & \mathrm{Q}_{\mathrm{tt}} \end{bmatrix}, \tag{23}$$

or proceed with a *one-time* Cholesky decomposition of $\mathrm{Q}_{\hat{\mathrm{x}}_0\hat{\mathrm{x}}_0} = \mathrm{G}_{\hat{\mathrm{x}}_0}\mathrm{G}_{\hat{\mathrm{x}}_0}^T$ and of $\mathrm{Q}_{\mathrm{tt}} = \mathrm{G}_{\mathrm{t}}\mathrm{G}_{\mathrm{t}}^T$ to set

$$\mathrm{U}_j = \begin{bmatrix} \mathrm{G}_{\hat{\mathrm{x}}_0}^{-1} & \mathrm{G}_{\hat{\mathrm{x}}_0}^{-1}\mathrm{L}_j \\ 0_{r\times n} & \mathrm{G}_{\mathrm{t}}^{-1} \end{bmatrix} \to \mathrm{Q}_{\mathrm{z}_j\mathrm{z}_j} = \begin{bmatrix} \mathrm{I}_n & 0_{n\times r} \\ 0_{r\times n} & \mathrm{I}_r \end{bmatrix}, \tag{24}$$

where $\mathrm{G}_{\hat{\mathrm{x}}_0}^{-1}$ is already obtained by solving the system of normal equations from (5) by making use of $\mathrm{A}^T\mathrm{Q}_{\mathrm{yy}}^{-1}\mathrm{A} = \mathrm{Q}_{\hat{\mathrm{x}}_0\hat{\mathrm{x}}_0}^{-1} = \mathrm{G}_{\hat{\mathrm{x}}_0}^{-T}\mathrm{G}_{\hat{\mathrm{x}}_0}^{-1}$. The option in (24) is preferred for moderate to high dimension of $\underline{\mathrm{s}}_j \in \mathbb{R}^{(n+r)}$ (e.g., > 5). Applying the change of variable from (24) to (20) we obtain

$$\mathbb{P}_{\mathcal{F}}|\mathcal{H} = \sum_{j=0}^{k} \underbrace{\mathsf{E}_{f_{\underline{\mathrm{z}}_j}}\left(\mathbb{1}_j\left(\mathrm{U}_j^{-1}\underline{\mathrm{z}}\right)|\mathcal{H}\right)}_{\mathcal{S}_j}, \tag{25}$$

where $\mathrm{U}_j^{-1} = \begin{bmatrix} \mathrm{G}_{\hat{\mathrm{x}}_0} & -\mathrm{L}_j\mathrm{G}_{\mathrm{t}} \\ 0_{r\times n} & \mathrm{G}_{\mathrm{t}} \end{bmatrix}$ and the number of distributional parameters of $f_{\underline{\mathrm{z}}_j}(z|\mathcal{H})$ is $2(n+r)$. Note that the dimensionality of the components $\mathcal{S}_j$ now increases *linearly* rather than quadratically, as was the case for $\mathcal{X}_j$ in (20). It is the expression in (25) that is used in the further developments and analysis.

The second step is to generate N_j independent and identically distributed (i.i.d.) pseudo-random samples from $f_{\underline{\mathrm{z}}_j}(z|\mathcal{H})$ to compute (25) via standard Monte Carlo (MC) [36],

$$\underline{\mathbb{P}}_{\mathcal{F}}|\mathcal{H} = \sum_{j=0}^{k} \underbrace{\left[\frac{1}{N_j}\sum_{\ell=1}^{N_j}\mathbb{1}_j\left(\mathrm{U}_j^{-1}\underline{\mathrm{z}}^{(\ell)}\right)\right]}_{\underline{\mathcal{S}}_j}. \tag{26}$$

where the underscores in $\underline{\mathbb{P}}_{\mathcal{F}}|\mathcal{H}$ and in $\underline{\mathcal{S}}_j$ indicate that the quantities have been numerically computed and thus includes simulation-related uncertainty. For simplicity we consider $N_j = N$ for all $j \in \{0, ..., k\}$. The component-wise mean and simulation variance (dispersion) are [44]

$$\mathsf{E}_f\left(\underline{\mathcal{S}}_j|\mathcal{H}\right) = \mathcal{S}_j, \quad \mathsf{D}_f\left(\underline{\mathcal{S}}_j|\mathcal{H}\right) = \frac{\mathcal{S}_j\left(1-\mathcal{S}_j\right)}{N}. \tag{27}$$

The results of $\mathsf{E}_f(.)$ and $\mathsf{D}_f(.)$ correspond to the Bernoulli distribution. If the objective is to compute a target value $\mathcal{S}_j = 10^{-9}$ with $\sqrt{\mathsf{D}_f\left(\underline{\mathcal{S}}_j|\mathcal{H}\right)} = 10^{-10}$, then the required number of pseudo-random samples would be $N \approx 10^{11}$. This illustrates the main challenge in rare-event simulation: the requirement for an extremely large number of pseudo-random samples to achieve a desired simulation standard deviation. To tackle this problem, a different approach from the standard MC method is needed.

Importance Sampling (IS) is a reasonable candidate to be considered as it can achieve simulation variance reduction without a significant increase of the required pseudo-random samples [37]. It has found applicability across a wide area of safety-critical applications, such as reliability analyses for structures, nuclear power plants, and for computation of probabilities of collision events in aviation [45]–[47]. Based on the principles of IS, the expected values in (25) can be re-expressed as

$$\mathbb{P}_{\mathcal{F}}|\mathcal{H} = \sum_{j=0}^{k} \underbrace{\mathsf{E}_{\tilde{f}_j}\left(\mathbb{1}_j\left(\mathrm{U}_j^{-1}\underline{\mathrm{z}}\right)\tilde{\mathcal{L}}_j\left(\underline{\mathrm{z}}\right)|\mathcal{H}\right)}_{\tilde{\mathcal{S}}_j}, \tag{28}$$

where $\tilde{\mathcal{L}}_j(\underline{\mathrm{z}}) = \dfrac{f_{\underline{\mathrm{z}}_j}\left(\underline{\mathrm{z}}|\mathcal{H}\right)}{\tilde{f}_j\left(\underline{\mathrm{z}}\right)}$. The newly introduced PDFs $\tilde{f}_j\left(z\right)$ are called IS densities, auxiliar densities, or proposal densities

[44], [48]. A necessary condition for the IS densities is $\mathbb{1}_j(\mathrm{U}_j^{-1}z)\tilde{f}_j(z) \neq 0$ whenever $\mathbb{1}_j(\mathrm{U}_j^{-1}z)f_{\underline{\mathrm{z}}_j}(z|\mathcal{H}) \neq 0$ [48]. Given $\tilde{N}_j = \tilde{N}$, for all $j \in \{0, ..., k\}$, i.i.d. pseudo-random samples generated from the IS densities $\tilde{f}_j(z)$, then (28) can be computed as

$$\underline{\mathbb{P}}_{\mathcal{F}}|\mathcal{H} = \sum_{j=0}^{k} \underbrace{\left[\frac{1}{\tilde{N}} \sum_{\ell=1}^{\tilde{N}} \mathbb{1}_j\left(\mathrm{U}_j^{-1}\underline{\mathrm{z}}^{(\ell)}\right) \tilde{\mathcal{L}}_j\left(\underline{\mathrm{z}}^{(\ell)}\right)\right]}_{\tilde{\mathcal{S}}_j}, \tag{29}$$

where $\underline{\mathbb{P}}_{\mathcal{F}}|\mathcal{H}$ is an unbiased estimator of $\mathbb{P}_{\mathcal{F}}(\mathbf{b})$ if the conditions for the IS densities are met [44], [48]. The simulation variance of the numerically computed j^{th} component $\underline{\tilde{\mathcal{S}}}_j$ is

$$\mathsf{D}_{\tilde{f}_j}\left(\underline{\tilde{\mathcal{S}}}_j|\mathcal{H}\right) = \frac{\left[\mathsf{E}_{\tilde{f}_j}\left(\mathbb{1}_j\left(\mathrm{U}_j^{-1}\underline{\mathrm{z}}\right)\tilde{\mathcal{L}}_j^2\left(\underline{\mathrm{z}}\right)|\mathcal{H}\right) - \tilde{\mathcal{S}}_j^2\right]}{\tilde{N}}, \tag{30}$$

which can be used as criteria for the choices of the IS densities to achieve variance reduction. One can notice from (30) that the following IS densities are giving *exactly* zero variances [37]

$$\tilde{f}_j^*(z) = \frac{\mathbb{1}_j\left(\mathrm{U}_j^{-1}z\right) f_{\underline{\mathrm{z}}_j}(z|\mathcal{H})}{\tilde{\mathcal{S}}_j}. \tag{31}$$

These theoretically optimal IS densities are the best in a minimum variance sense. However, as they depend on the unknown quantities of interest, their use is not feasible in practice. Instead, one could search within a parametric family of PDFs (e.g., exponential family) and find the one that minimizes (30) [44]. We account for the distributional parameters in the notation of $\tilde{f}_j(z;\tilde{\Theta}_j)$ and formulate the following variance minimization problem [49]

$$\underline{\tilde{\Theta}}_j = \arg\min_{\tilde{\Theta}_j} \mathsf{E}_{\tilde{f}_j}\left(\mathbb{1}_j\left(\mathrm{U}_j^{-1}\underline{\mathrm{z}}\right)\frac{f_{\underline{\mathrm{z}}_j}^2(\underline{\mathrm{z}}|\mathcal{H})}{\tilde{f}_j^2\left(\underline{\mathrm{z}};\tilde{\Theta}_j\right)}\right). \tag{32}$$

Typically there are no analytical solutions to the minimization problems in (32), and this can lead to time consuming optimization algorithms [38]. In [38], Rubinstein proposes an alternative which is based on finding the IS densities which minimizes the cross-entropy, or Kullback-Leibler (KL) divergence, w.r.t. the theoretically optimal IS densities in (31). The KL divergences are defined as [50]

$$\mathcal{D}\left(\tilde{f}_j^*, \tilde{f}_j\right) = \mathsf{E}_{\tilde{f}_j^*}\left(\ln \tilde{f}_j^*(\underline{\mathrm{z}})\right) - \mathsf{E}_{\tilde{f}_j^*}\left(\ln \tilde{f}_j(\underline{\mathrm{z}};\tilde{\Theta}_j)\right). \tag{33}$$

Using the expressions of the theoretically optimal IS densities from (31), the minimization problem of (33) w.r.t. $\tilde{\Theta}_j$ becomes

$$\underline{\tilde{\Theta}}_j = \arg\min_{\tilde{\Theta}_j} -\mathsf{E}_{f_{\underline{\mathrm{z}}_j}}\left(\mathbb{1}_j\left(\mathrm{U}_j^{-1}\underline{\mathrm{z}}\right)\ln \tilde{f}_j\left(\underline{\mathrm{z}};\tilde{\Theta}_j\right)|\mathcal{H}\right). \tag{34}$$

Note that the expected values in (34) are now expressed w.r.t. the original PDFs $f_{\underline{\mathrm{z}}_j}(z|\mathcal{H})$, which means that the minimization problems may be too computationally expensive to be carried out in the context of rare events since $\mathbb{1}_j\left(\mathrm{U}_j^{-1}\underline{\mathrm{z}}\right) = 0$ too often. To circumvent this issue, the expected values can be expressed with respect to newly introduced IS densities $\acute{f}_j(z;\acute{\Theta}_j)$ (assumed to be known a-priori) [38]

$$\underline{\tilde{\Theta}}_j = \arg\max_{\tilde{\Theta}_j} \mathsf{E}_{\acute{f}_j}\left(\mathbb{1}_j\left(\mathrm{U}_j^{-1}\underline{\mathrm{z}}\right)\frac{f_{\underline{\mathrm{z}}_j}(\underline{\mathrm{z}}|\mathcal{H})}{\acute{f}_j(\underline{\mathrm{z}};\acute{\Theta}_j)}\ln \tilde{f}_j\left(\underline{\mathrm{z}};\tilde{\Theta}_j\right)\right). \tag{35}$$

The stochastic counterpart of (35) can be formulated given access $\acute{N}_j$ pseudo-random samples from the a-priori IS densities $\acute{f}_j(z;\acute{\Theta}_j)$,

$$\underline{\tilde{\Theta}}_j = \arg\max_{\tilde{\Theta}_j} \frac{1}{\acute{N}_j}\sum_{\ell=1}^{\acute{N}_j} \mathbb{1}_j\left(\mathrm{U}_j^{-1}\underline{\mathrm{z}}^{(\ell)}\right)\acute{\mathcal{L}}_j(\underline{\mathrm{z}}^{(\ell)})\ln \tilde{f}_j\left(\underline{\mathrm{z}}^{(\ell)};\tilde{\Theta}_j\right), \tag{36}$$

$\acute{\mathcal{L}}_j(\underline{\mathrm{z}}^{(\ell)}) = \dfrac{f_{\underline{\mathrm{z}}_j}(\underline{\mathrm{z}}^{(\ell)})}{\acute{f}_j(\underline{\mathrm{z}}^{(\ell)};\acute{\Theta}_j)}$. If the objective functions in (36) are convex and differentiable $\tilde{\Theta}_j$, the solutions may be obtained analytically by setting the gradients to zero [38], [44]. A procedure, known as the Cross-Entropy (CE) method, can be used to carry out the maximization problems in (36) as described in [51], [52]. Once $\underline{\tilde{\Theta}}_j$ are obtained, then $\tilde{N}$ i.i.d. pseudo-random samples can be generated from $\tilde{f}_j(z;\underline{\tilde{\Theta}}_j)$ to compute (29).

The third step quantifies the uncertainty related to the simulation. This is achieved by repeating the computations of the second step N_{sim} times, each time with a different set of i.i.d. pseudo-random samples. The results are the mean values of the components $\underline{\tilde{\mathcal{M}}}_j = (1/N_{\text{sim}})\sum_{h=1}^{N_{\text{sim}}}\underline{\tilde{\mathcal{S}}}_j^{(h)}$, and the empirical standard deviations $\tilde{\sigma}_j$, based on which $\overline{\underline{\mathbb{P}}}_{\mathcal{F}}|\mathcal{H} = \sum_{j=0}^{k}\underline{\tilde{\mathcal{M}}}_j$ and its σ_{sim} are obtained. Some common example values for N_{sim} are 50, 100 [53], [54]. The three-step procedure to compute the Level 1 components in Fig. 2 is summarized in Fig. 3.

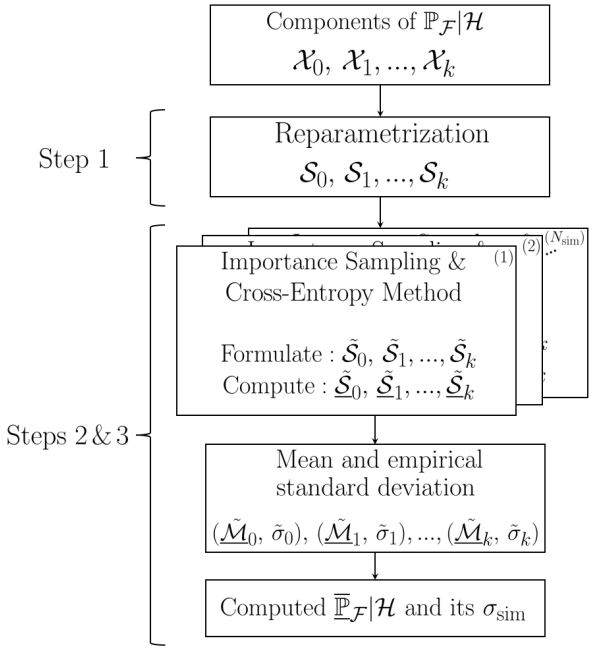

Fig. 3. Summary of procedure to compute Level 1 components in Fig. 2.

B. Computation of Level 2 Component

Once the Level 1 entries $\overline{\underline{\mathbb{P}}}_{\mathcal{F}}|\mathcal{H}_0,...,\overline{\underline{\mathbb{P}}}_{\mathcal{F}}|\mathcal{H}_k(\mathrm{b}_k)$ and their simulation standard deviations are obtained, one needs to make assumptions or have knowledge of the a priori probabilities of occurrences of the hypotheses $\mathsf{P}(\mathcal{H}_0),...,\mathsf{P}(\mathcal{H}_k)$. Assuming access to their values, then the total probability of positioning failure can be computed

$$\overline{\underline{\mathbb{P}}}_{\mathcal{F}}(\mathbf{b}) = \mathsf{P}(\mathcal{H}_0)\overline{\underline{\mathbb{P}}}_{\mathcal{F}}|\mathcal{H}_0 + \sum_{i=1}^{k} \mathsf{P}(\mathcal{H}_i)\overline{\underline{\mathbb{P}}}_{\mathcal{F}}|\mathcal{H}_i(\mathrm{b}_i) \tag{37}$$

and its simulation standard deviation propagated accordingly. For positioning safety analyses, the maximum of (37) can be compared against an application specific requirement to decide whether the requirement is met,

$$\max_{\mathbf{b}} \overline{\underline{\mathbb{P}}}_{\mathcal{F}}(\mathbf{b}) = \mathsf{P}(\mathcal{H}_0)\overline{\underline{\mathbb{P}}}_{\mathcal{F}}|\mathcal{H}_0 + \max_{\mathrm{b}_1,...,\mathrm{b}_k} \sum_{i=1}^{k} \mathsf{P}(\mathcal{H}_i)\overline{\underline{\mathbb{P}}}_{\mathcal{F}}|\mathcal{H}_i(\mathrm{b}_i). \tag{38}$$

C. Remarks on the family of PDFs to consider for the IS densities

When choosing the parametric family of PDFs for determining the IS densities using the CE method, a reasonable choice is to use the same parametric family as the original PDFs [51]. For example, if $f_{\underline{\mathrm{z}}_i}(z|\mathcal{H})$ is a Gaussian PDF, then choosing $\tilde{f}_i(z;\tilde{\Theta}_i)$ from the Gaussian family of PDFs is also reasonable. However, additional criteria should be taken into account when choosing the parametric family of PDFs for the IS densities, such as: the dimensionality of the vectors of interest (e.g., $\underline{\mathrm{x}} \in \mathbb{R}^n$, $\underline{\mathrm{t}} \in \mathbb{R}^r$), the characteristics of the safety (or failure)-regions (e.g., unimodal or multimodal), simulation time budget [55]–[57] etc. The detailed analysis of these aspects is beyond the scope of this contribution. In Section IV, we choose the parametric family of Gaussian PDFs for IS densities as $f_{\underline{\mathrm{z}}_i}(z|\mathcal{H})$ is also a Gaussian PDF for $i \in \{0,...,k\}$.

IV. Positioning Safety Analysis for an Automated Vehicle

As an example, to demonstrate the working of the method we carry out a positioning safety analysis for an automated vehicle which coordinates, in a local East-North-Up (ENU) coordinate system, are determined using single-frequency (code)pseudorange observables in a Differential GNSS (DGNSS) setting. The GNSS constellations we consider are GPS (G) and Galileo (E), at L1/E1 radio-frequency (1575.42 MHz). A reference receiver is stationed at an accurately known position which determines the pseudorange corrections (PRCs) that are transmitted to the automated vehicle's rover receiver using a Networked Transport of RTCM via Internet Protocol (NTRIP) [58]. Depending on the distance between the reference and the rover receiver, decimeter-level positioning precision of the rover receiver is achievable [59]. An illustration of the DGNSS setup is presented in Fig. 4. The index '$*$' is used to indicate the GNSS constellation (G or E). The corresponding linear(ized) DGNSS model is given by [62]

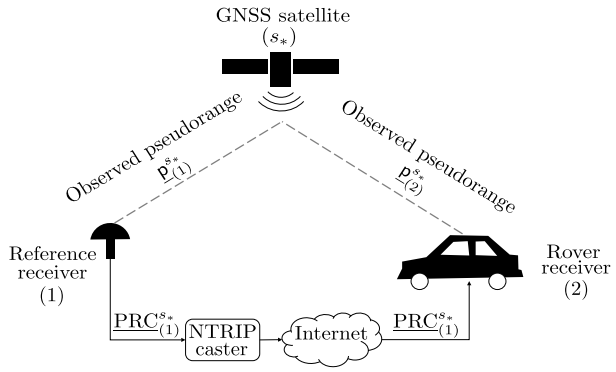

Fig. 4. Pseudorange corrections are determined at the reference receiver $\underline{\mathrm{PRC}}^{s_*}_{(1)} = \rho^{s_*}_{(1)} - \underline{\mathrm{p}}^{s_*}_{(1)}$, where $\rho^{s_*}_{(1)}$ is the Euclidean distance. The $\underline{\mathrm{PRC}}^{s_*}_{(1)}$'s are collected by an NTRIP caster which are then distributed to the automated vehicle's rover receiver to be applied to $\underline{\mathrm{p}}^{s_*}_{(2)}$. Source: Adapted from [60].

$$\begin{aligned} \mathsf{E}_{f_{\Delta\underline{\mathrm{y}}}}\underbrace{\left(\begin{bmatrix}\Delta\underline{\mathrm{y}}_{\mathrm{G}}\\ \Delta\underline{\mathrm{y}}_{\mathrm{E}}\end{bmatrix}\right)}_{\Delta\underline{\mathrm{y}}} &= \underbrace{\begin{bmatrix}\mathrm{M}_{\mathrm{G}} & \mathbf{u}_{\mathrm{G}}\\ \mathrm{M}_{\mathrm{E}} & \mathbf{u}_{\mathrm{E}}\end{bmatrix}}_{\mathrm{J_A}}\underbrace{\begin{bmatrix}\Delta\mathbf{r}\\ \mathsf{c}\,\Delta\mathbf{t}\end{bmatrix}}_{\Delta\mathrm{x}}, \\ \mathrm{Q}_{\Delta\mathrm{y}\Delta\mathrm{y}} &= \mathrm{blkdiag}[\mathrm{Q}_{\Delta\mathrm{y_G}\Delta\mathrm{y_G}}, \mathrm{Q}_{\Delta\mathrm{y_E}\Delta\mathrm{y_E}}], \end{aligned} \tag{39}$$

where $\Delta\underline{\mathrm{y}} \sim \mathcal{N}(\mathsf{E}_{f_{\Delta\underline{\mathrm{y}}}}(\Delta\underline{\mathrm{y}}), \mathrm{Q}_{\Delta\mathrm{y}\Delta\mathrm{y}})$ and $\mathrm{J_A} \in \mathbb{R}^{m\times n}$ is the Jacobian of the vector function $\mathrm{A}(.)$ which links the unknowns of interest to the nonlinear (code)pseudorange observables. The components of $\Delta\underline{\mathrm{y}}_* \in \mathbb{R}^{m_*}$ are the observed pseudoranges from which the Euclidean distances between an appropriately chosen linearization point and the satellites are subtracted, and the PRCs are applied via addition. The PRCs remove most of the satellite orbit errors, the satellite clock error and satellite code hardware bias, while the differential delays due to the troposphere and ionosphere are considered negligible for distances between the reference and rover receiver up to 10 km [61]. Both the reference and rover receivers have calibrated the GPS-Galileo Inter System Bias (ISB) by applying it as an additional correction to their pseudoranges [62]. The rows of $\mathrm{M}_* \in \mathbb{R}^{m_*\times 3}$ contain the unit direction vectors between the rover receiver and the satellites, while $\mathbf{u}_* \in \mathbb{R}^{m_*}$ is the vector of ones. The unknown parameters are the rover's ENU coordinate increments $\Delta\mathbf{r} \in \mathbb{R}^3$ and $\Delta\mathbf{t} \in \mathbb{R}$ which represents the combined differential receiver clock and hardware delay. The c term is the speed of light in a vacuum. The Jacobian $\mathrm{J_A} \in \mathbb{R}^{m\times n}$ has $\mathrm{rank}(\mathrm{J_A}) = 4$. The variance-covariance matrix $\mathrm{Q}_{\Delta\mathrm{y}_*\Delta\mathrm{y}_*} = 2\sigma^2_{\mathrm{y}_*}\mathrm{W}^{-1}_* \in \mathbb{R}^{m_*\times m_*}$ is diagonal where $\mathrm{W}_* = \mathrm{diag}[\omega_{1_*},...,\omega_{m_*}] \in \mathbb{R}^{m_*\times m_*}$ is the weight matrix which components are the elevation-dependent weighting functions based on [63]. In $\mathrm{Q}_{\Delta\mathrm{y}_*\Delta\mathrm{y}_*}$, σ_{y_*} is the standard deviation of the pseudorange observables, in [m], and the factor 2 is due to the application of the PRCs to the observed pseudoranges by the rover receiver (assuming the same σ_{y_*} at both reference and rover receivers [64]). In this scenario, we aim for a horizontal positioning precision of approximately 0.5 meters, specified as the 95% circular probability radius.

To achieve this, we set $\sqrt{2}\sigma_{\mathrm{y_G}} = 0.3$ m and $\sqrt{2}\sigma_{\mathrm{y_E}} = 0.2$ m, which correspond to positioning precision attainable with DGNSS [59].

The model in (39) has a total number of $m = m_{\mathrm{G}} + m_{\mathrm{E}}$ observables and $n = 4$ unknowns. The redundancy follows to be $r = m - \mathrm{rank}(\mathrm{J_A}) = m - 4$. The estimate $\hat{\mathrm{x}}$ is obtained from a Gauss-Newton iteration scheme once the stop criterion is met for $\Delta\hat{\mathrm{x}}$ [65]. Given that $r \geq 2$, we account for individual outliers in the observations (e.g., due to signal reflections by local environment near the rover receiver) and assume that only one observation outlier occurs at a time. This is the case of datasnooping [66], [67]. The following statistical hypothesis testing problem is defined

$$\mathcal{H}_0 : \mathsf{E}_{f_{\Delta\underline{\mathrm{y}}}}\left(\Delta\underline{\mathrm{y}}\right) = \mathrm{J_A}\Delta\mathrm{x} \text{ vs. } \mathcal{H}_i : \mathsf{E}_{f_{\Delta\underline{\mathrm{y}}}}\left(\Delta\underline{\mathrm{y}}\right) = \mathrm{J_A}\Delta\mathrm{x} + \mathrm{c}_i\mathrm{b}_i \tag{40}$$

for $i \in \{1, ..., k\}$, where $k = m$, $\mathrm{c}_i \in \mathbb{R}^m$ is the canonical unit vector having one as its i^{th} element and zero elsewhere, $\mathrm{b}_i \in \mathbb{R}$ is the unknown outlier with its size in [m], and $\mathrm{rank}([\mathrm{J_A}, \mathrm{c}_i]) = 4 + 1 = 5$. Given the misclosure vector $\underline{\mathrm{t}} = \mathrm{B}^T\Delta\underline{\mathrm{y}}$ with $\mathrm{B}^T\mathrm{J_A} = 0_{r\times n}$, the resulting partitions of $\mathbb{R}^r$ for datasnooping, given a level of significance $\alpha = \mathsf{P}_{\mathrm{FA}}$ are

$$\mathcal{P}_0 = \left\{t \in \mathbb{R}^r \mid ||t||^2_{\mathrm{Q_{tt}}} \leq \chi^2_\alpha(r, 0)\right\}, \tag{41}$$

$$\mathcal{P}_{i\neq 0} = \left\{t \in \mathbb{R}^r \mid t \notin \mathcal{P}_0,\ |w_i| = \max_{j\in\{1,\ldots,k\}} |w_j|\right\}, \tag{42}$$

where $|\underline{w}_j| = ||\mathbf{\Pi}_{\mathrm{c}_{t_j}}\underline{\mathrm{t}}||_{\mathrm{Q_{tt}}}$ is the w-test statistic [68].

We consider the skyplot in Fig. 5 which shows the positions of the satellites, as observed by the rover receiver, expressed in terms of their azimuth (w.r.t. the North direction) and elevation angles (w.r.t. the horizontal plane).

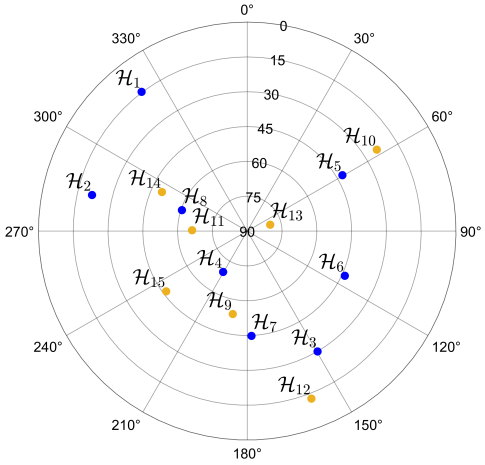

Fig. 5. Skyplot view of the rover receiver (vehicle)-satellite geometry. The eight blue dots are representing the GPS satellites, while the seven orange ones represents the Galileo satellites and the corresponding $\mathcal{H}_i$'s, for $i > 0$.

The satellite geometry contains $m_{\mathrm{G}} = 8$ GPS satellites (blue) and $m_{\mathrm{E}} = 7$ Galileo satellites (orange) with an elevation cut-off angle of $10°$. The redundancy is $r = 11$ and the analysis focuses on the 2D position of the vehicle as the horizontal domain is most relevant. The 2D position vector is defined as $\overline{\theta} = \mathrm{H}^T\overline{\mathrm{x}}$ where $\mathrm{H}^T = \begin{bmatrix}\mathrm{I}_2 & 0_{2\times 2}\end{bmatrix}$ and $\overline{\mathrm{x}} = \sum_{i=0}^{k=15} \hat{\underline{\mathrm{x}}}_i p_i(\underline{\mathrm{t}})$ captures the estimation and statistical hypothesis testing problem defined in (40)–(42). The PDF of $\overline{\theta}$ can be expressed as [18]

$$\begin{aligned} f_{\overline{\theta}}(\theta) &= \sum_{i=0}^{k=15} \int_{\mathcal{P}_i} f_{\hat{\underline{\theta}}_i, \underline{\mathrm{t}}}(x, t)\, dt \\ &= \sum_{i=0}^{k=15} \mathsf{E}_{f_{\underline{\mathrm{t}}}}\left(f_{\hat{\underline{\theta}}_0}\left(\theta + \mathrm{H}^T\mathrm{L}_i\,\underline{\mathrm{t}}\right) p_i(\underline{\mathrm{t}})\right), \end{aligned} \tag{43}$$

where the second equality will be used for the visual interpretation of the PDFs. Based on (43), the 2D probability of positioning failure is formulated with the objective of computing it using the proposed method from Section III

$$\mathbb{P}_{\mathcal{F}}(\mathbf{b}) = \int_{\mathcal{B}^c} f_{\overline{\theta}}(\theta)\, d\theta, \tag{44}$$

for a given safety region $\mathcal{B}$ and its complement $\mathcal{B}^c$.

A. Probability of positioning failure for fixed vehicle and safety-region orientation

In determining the shape and size of the safety region $\mathcal{B} \subset \mathbb{R}^2$, several factors should be considered, such as: (i) the vehicle's dimensions; (ii) the road geometry to ensure that all points $\theta \in \mathbb{R}^2$ within the set $\mathcal{B}$ correspond to the vehicle staying within its lane; (iii) the minimum required braking distance depending on the vehicle's speed; (iv) the proximity to other traffic participants, among other considerations. Various studies have proposed different shapes for the safety region that encompasses the vehicle, such as elliptical or rectangular forms [7], [69], [70]. For consistency with existing approaches in the literature, we choose an ellipse to inscribe the shape of the vehicle which has a length of 4.5 [m], a width of 1.8 [m], and the orientation w.r.t. the vertical (north) axis is $45°$ (as an example).

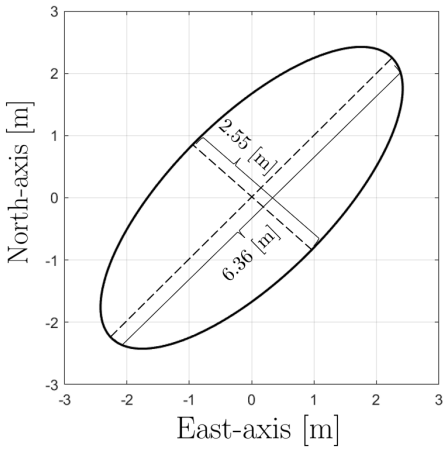

Fig. 6. Safety-region $\mathcal{B} \subset \mathbb{R}^2$ inscribing the vehicle (at a single-epoch) defined in (45).

For a single epoch in time, the safety region can be defined as (see Fig. 6),

$$\mathcal{B} = \{\theta \in \mathbb{R}^2 \mid ||\theta - \theta_{\text{true}}||^2_{\mathrm{Q_B}} \leq 1\}, \tag{45}$$

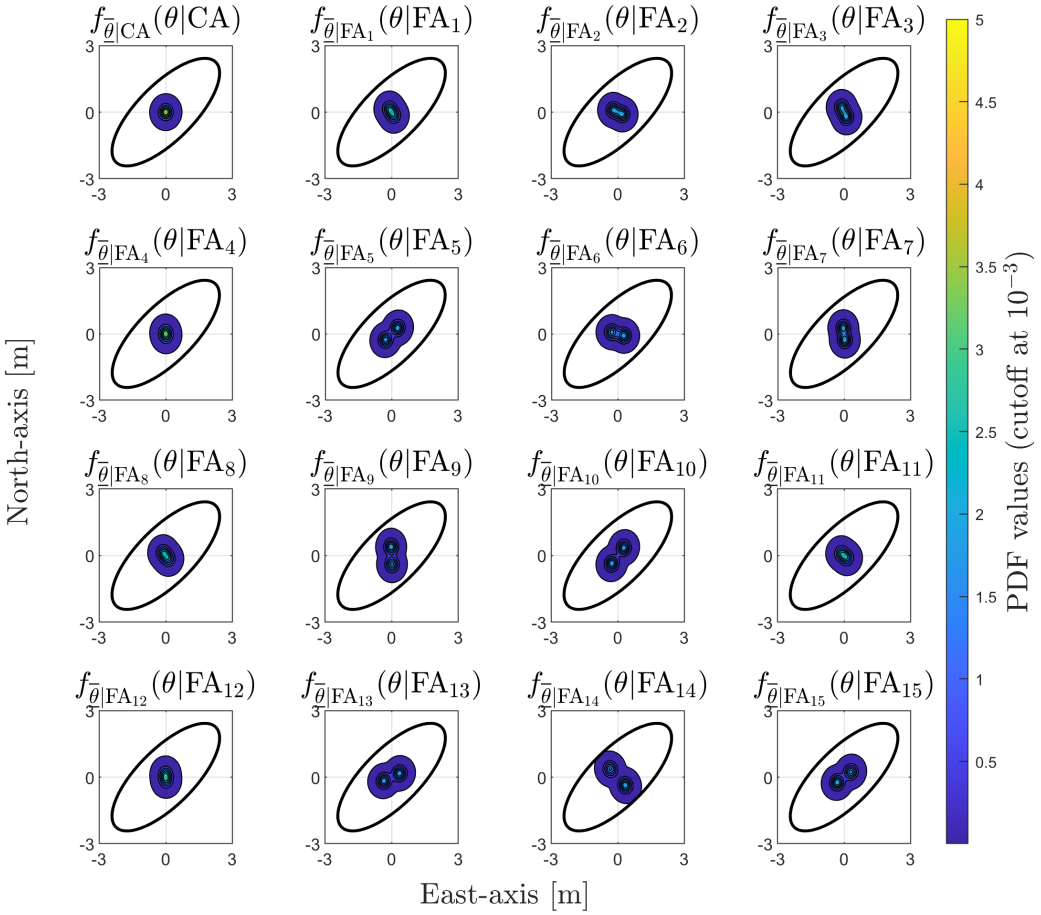

Fig. 7. Components of $f_{\underline{\theta}}(\theta|\mathcal{H}_0)$ for $\mathrm{P_{FA}} = 10^{-3}$ and $N_\mathrm{t} = 10^7$ i.i.d. pseudo-random samples drawn from $f_{\underline{t}}(t|\mathcal{H}_0)$. The ellipse represents the safety-region $\mathcal{B} \subset \mathbb{R}^2$ from (45) in relation with each conditional component of $f_{\underline{\theta}}(\theta|\mathcal{H}_0)$ (i.e., $f_{\underline{\theta}|\mathrm{CA}}(\theta|\mathrm{CA})$ and $f_{\underline{\theta}|\mathrm{FA}_i}(\theta|\mathrm{FA}_i)$ for $i \in \{1, ..., 15\}$.

where $\mathrm{Q}_{\mathcal{B}}^{-1} = \begin{bmatrix} 0.358 & -0.259 \\ -0.259 & 0.358 \end{bmatrix}$ $[\mathrm{m}^{-2}]$ and $\theta_{\text{true}} \in \mathbb{R}^2$ is the true location of the vehicle (set at $0_{2\times1}$ for this example). The major-axis of $\mathcal{B}$ has a length of 6.36 [m] with an orientation w.r.t. the horizontal axis of 45°, and the minor-axis has a length of 2.55 [m]. In the following sub-sections (A.1 and A.2) we present results from computing the Level 1 components of $\overline{\mathbb{P}}_{\mathcal{F}}|\mathcal{H}_0$ and of $\overline{\mathbb{P}}_{\mathcal{F}}|\mathcal{H}_{14}$ as illustrative examples. A similar approach is followed for the remaining fourteen Level 1 entries $\overline{\mathbb{P}}_{\mathcal{F}}|\mathcal{H}_i$ for $i \notin \{0, 14\}$. In sub-section (A.3) the resulting total probability of positioning failure is obtained and discussed.

A.1 Computation of Level 1 Components of $\mathbb{P}_{\mathcal{F}}|\mathcal{H}_0$

First, we are providing an analysis of the conditional components of the PDF $f_{\underline{\theta}}(\theta|\mathcal{H}_0)$ (i.e., $f_{\underline{\theta}|\mathrm{CA}}(\theta|\mathrm{CA})$ and $f_{\underline{\theta}|\mathrm{FA}_i}(\theta|\mathrm{FA}_i)$ for $i \in \{1, ..., 15\}$). Under the event of a CA testing decision, the PDF $f_{\underline{\theta}|\mathrm{CA}}(\theta|\mathrm{CA}) = f_{\underline{\hat{\theta}}_0}(\theta|\mathcal{H}_0)$ is a normal distribution, with the precision of the horizontal position components $\sigma_{\hat{\theta}_0,\text{east}} = 0.18$ [m], $\sigma_{\hat{\theta}_0,\text{north}} = 0.20$ [m], and the correlation coefficient is $\rho_{\hat{\theta}_0} = 0.01$. Hence, the contours of $f_{\underline{\theta}|\mathrm{CA}}(\theta|\mathrm{CA})$ are nearly circular. The conditional PDFs $f_{\underline{\theta}|\mathrm{FA}_i}(\theta|\mathrm{FA}_i)$ are obtained from the averaged shifted functions $f_{\underline{\hat{\theta}}_0}\left(\theta + \mathrm{H}^T\mathrm{L}_i\,\underline{\mathrm{t}}|\mathcal{H}_0\right)$ for $\underline{\mathrm{t}} \in \mathcal{P}_i$, which account for the outcome of statistical testing (see (43)). A closer look into the shifting term $\mathrm{H}^T\mathrm{L}_i\,\underline{\mathrm{t}}$ will give better insights about the features of $f_{\underline{\theta}|\mathrm{FA}_i}(\theta|\mathrm{FA}_i)$ (e.g., orientation, multimodality). We re-express the shifting term, for $i > 0$, as

$$\mathrm{H}^T\mathrm{L}_i\,\underline{\mathrm{t}} = \mathrm{H}^T\mathrm{Q}_{\hat{\mathrm{x}}_0\hat{\mathrm{x}}_0}\mathrm{J}_\mathrm{A}^T\mathrm{Q}^{-1}_{\Delta\mathrm{y}\Delta\mathrm{y}}\mathrm{c}_i\,(\mathrm{c}_{\mathrm{t}_i}^+\,\underline{\mathrm{t}}) = \mathrm{g}_i\,(\mathrm{c}_{\mathrm{t}_i}^+\,\underline{\mathrm{t}}), \quad (46)$$

where $\mathrm{g}_i \in \mathbb{R}^2$ and $(\mathrm{c}_{\mathrm{t}_i}^+\,\underline{\mathrm{t}}) \in \mathbb{R}$. The angle of $\mathcal{R}(\mathrm{g}_i)$ w.r.t. the horizontal axis is driven by the design matrix $\mathrm{J_A}$ and by $\mathrm{Q}_{\Delta\mathrm{y}_*\Delta\mathrm{y}_*}$ through $\mathrm{Q}_{\hat{\mathrm{x}}_0\hat{\mathrm{x}}_0}$. The rows of $(\mathrm{H}^T\mathrm{Q}_{\hat{\mathrm{x}}_0\hat{\mathrm{x}}_0}) \in \mathbb{R}^{2\times n}$ (variances of the components on East and North directions, the covariance between them, and their covariances with the Up component and $\Delta\mathbf{t}$) are influencing the orientation of $\mathcal{R}(\mathrm{g}_i)$ by transforming the scaled rows of $\mathrm{J_A}$ obtained from $(\mathrm{J}_\mathrm{A}^T\mathrm{Q}^{-1}_{\Delta\mathrm{y}\Delta\mathrm{y}}\mathrm{c}_i) \in \mathbb{R}^n$. In turn, $\mathcal{R}(\mathrm{g}_i)$ drives the orientation of $f_{\underline{\theta}|\mathrm{FA}_i}(\theta|\mathrm{FA}_i)$. One can relate the satellite geometry from Fig. 5 with the components in Fig. 7 to identify which ones present similarities (e.g., in orientation and shape). As examples, the following 'pairs' of components show similarities: $f_{\underline{\theta}|\mathrm{FA}_5}(\theta|\mathrm{FA}_5)$ and $f_{\underline{\theta}|\mathrm{FA}_{10}}(\theta|\mathrm{FA}_{10})$, $f_{\underline{\theta}|\mathrm{FA}_8}(\theta|\mathrm{FA}_8)$ and $f_{\underline{\theta}|\mathrm{FA}_{11}}(\theta|\mathrm{FA}_{11})$, $f_{\underline{\theta}|\mathrm{FA}_7}(\theta|\mathrm{FA}_7)$ and $f_{\underline{\theta}|\mathrm{FA}_9}(\theta|\mathrm{FA}_9)$, etc. The way $(\mathrm{c}_{\mathrm{t}_i}^+\,\underline{\mathrm{t}})$ varies across $\mathcal{R}(\mathrm{g}_i)$, for $\underline{\mathrm{t}} \in \mathcal{P}_i$, determines the multimodality of $f_{\underline{\theta}|\mathrm{FA}_i}(\theta|\mathrm{FA}_i)$. Take, for example, $f_{\underline{\theta}|\mathrm{FA}_1}(\theta|\mathrm{FA}_1)$ and $f_{\underline{\theta}|\mathrm{FA}_{12}}(\theta|\mathrm{FA}_{12})$ as they do not show multimodality due to the reduced influence of the low-elevation satellites 1 and 12 on the 2D positioning (via

the elevation-based weighting in $\mathrm{Q}_{\Delta \mathrm{y}_*\Delta \mathrm{y}_*}$). The components $f_{\underline{\theta}|\mathrm{FA}_4}(\theta|\mathrm{FA}_4)$, $f_{\underline{\theta}|\mathrm{FA}_8}(\theta|\mathrm{FA}_8)$, and $f_{\underline{\theta}|\mathrm{FA}_{11}}(\theta|\mathrm{FA}_{11})$ do not show multimodality, despite satellites 4, 8, and 11 being at a rather high elevation, because of their reduced contribution to the east and north directions. The rest of the components show multimodality as the corresponding satellites' contribution to the 2D positioning is larger due to the rover receiver-satellite geometry and due to the elevation weighting. By relating the shape of the safety-region $\mathcal{B}$ with these components (see Fig. 7) it is possible to identify which ones have a small or large amount of probability density outside $\mathcal{B}$. For instance, $f_{\underline{\theta}|\mathrm{FA}_{14}}(\theta|\mathrm{FA}_{14})$ is closely aligned with the minor-axis of $\mathcal{B}$ and its modes are the furthest apart, which indicates that it is one of the components with the largest amount of probability density outside $\mathcal{B}$.

Secondly, we compute the Level 1 components corresponding to $\mathcal{H}_0$ using the procedure in Fig. 3

$$\overline{\underline{\mathbb{P}}}_{\mathcal{F}}|\mathcal{H}_0 = \sum_{i=0}^{k=15} \underline{\tilde{\mathcal{M}}}_i|\mathcal{H}_0 = \mathsf{P}_{\mathrm{CA}}\tilde{\underline{\mathbb{P}}}_{\mathcal{F}}|\mathrm{CA} + \sum_{i=1}^{k=15} \tilde{\underline{\mathsf{P}}}_{\mathrm{FA}_i}\tilde{\underline{\mathbb{P}}}_{\mathcal{F}}|\mathrm{FA}_i, \tag{47}$$

where P_{CA} is known, since $\mathsf{P}_{\mathrm{CA}} = 1 - \mathsf{P}_{\mathrm{FA}} = 1 - 10^{-3}$. The results are obtained over $N_{\mathrm{sim}} = 100$ displayed in Table I.

TABLE I
LEVEL 1 COMPONENTS OF $\overline{\underline{\mathbb{P}}}_{\mathcal{F}}|\mathcal{H}_0$ FOR $\mathsf{P}_{\mathrm{FA}} = 10^{-3}$ AND $\tilde{N}_i = 10^5$ I.I.D. PSEUDO-RANDOM SAMPLES DRAWN FROM IS DENSITIES. RESULTS ARE OBTAINED OVER $N_{\mathrm{SIM}} = 100$.

Comp.	Value	Std.
$\mathsf{P}_{\mathrm{CA}}\tilde{\underline{\mathbb{P}}}_{\mathcal{F}}\|\mathrm{CA}$	$2.51 \cdot 10^{-11}$	$6.39 \cdot 10^{-14}$
$\tilde{\underline{\mathsf{P}}}_{\mathrm{FA}_1}\tilde{\underline{\mathbb{P}}}_{\mathcal{F}}\|\mathrm{FA}_1$	$4.63 \cdot 10^{-13}$	$1.04 \cdot 10^{-14}$
$\tilde{\underline{\mathsf{P}}}_{\mathrm{FA}_2}\tilde{\underline{\mathbb{P}}}_{\mathcal{F}}\|\mathrm{FA}_2$	$1.29 \cdot 10^{-12}$	$2.80 \cdot 10^{-14}$
$\tilde{\underline{\mathsf{P}}}_{\mathrm{FA}_3}\tilde{\underline{\mathbb{P}}}_{\mathcal{F}}\|\mathrm{FA}_3$	$2.55 \cdot 10^{-12}$	$5.42 \cdot 10^{-14}$
$\tilde{\underline{\mathsf{P}}}_{\mathrm{FA}_4}\tilde{\underline{\mathbb{P}}}_{\mathcal{F}}\|\mathrm{FA}_4$	$1.73 \cdot 10^{-14}$	$7.76 \cdot 10^{-16}$
$\tilde{\underline{\mathsf{P}}}_{\mathrm{FA}_5}\tilde{\underline{\mathbb{P}}}_{\mathcal{F}}\|\mathrm{FA}_5$	$2.20 \cdot 10^{-15}$	$9.42 \cdot 10^{-17}$
$\tilde{\underline{\mathsf{P}}}_{\mathrm{FA}_6}\tilde{\underline{\mathbb{P}}}_{\mathcal{F}}\|\mathrm{FA}_6$	$4.48 \cdot 10^{-12}$	$7.25 \cdot 10^{-14}$
$\tilde{\underline{\mathsf{P}}}_{\mathrm{FA}_7}\tilde{\underline{\mathbb{P}}}_{\mathcal{F}}\|\mathrm{FA}_7$	$2.56 \cdot 10^{-12}$	$4.40 \cdot 10^{-14}$
$\tilde{\underline{\mathsf{P}}}_{\mathrm{FA}_8}\tilde{\underline{\mathbb{P}}}_{\mathcal{F}}\|\mathrm{FA}_8$	$4.82 \cdot 10^{-13}$	$1.04 \cdot 10^{-14}$
$\tilde{\underline{\mathsf{P}}}_{\mathrm{FA}_9}\tilde{\underline{\mathbb{P}}}_{\mathcal{F}}\|\mathrm{FA}_9$	$2.76 \cdot 10^{-11}$	$3.19 \cdot 10^{-13}$
$\tilde{\underline{\mathsf{P}}}_{\mathrm{FA}_{10}}\tilde{\underline{\mathbb{P}}}_{\mathcal{F}}\|\mathrm{FA}_{10}$	$1.56 \cdot 10^{-14}$	$3.54 \cdot 10^{-16}$
$\tilde{\underline{\mathsf{P}}}_{\mathrm{FA}_{11}}\tilde{\underline{\mathbb{P}}}_{\mathcal{F}}\|\mathrm{FA}_{11}$	$2.38 \cdot 10^{-13}$	$6.29 \cdot 10^{-15}$
$\tilde{\underline{\mathsf{P}}}_{\mathrm{FA}_{12}}\tilde{\underline{\mathbb{P}}}_{\mathcal{F}}\|\mathrm{FA}_{12}$	$6.82 \cdot 10^{-14}$	$2.20 \cdot 10^{-15}$
$\tilde{\underline{\mathsf{P}}}_{\mathrm{FA}_{13}}\tilde{\underline{\mathbb{P}}}_{\mathcal{F}}\|\mathrm{FA}_{13}$	$7.95 \cdot 10^{-14}$	$3.81 \cdot 10^{-15}$
$\tilde{\underline{\mathsf{P}}}_{\mathrm{FA}_{14}}\tilde{\underline{\mathbb{P}}}_{\mathcal{F}}\|\mathrm{FA}_{14}$	$4.86 \cdot 10^{-9}$	$4.36 \cdot 10^{-11}$
$\tilde{\underline{\mathsf{P}}}_{\mathrm{FA}_{15}}\tilde{\underline{\mathbb{P}}}_{\mathcal{F}}\|\mathrm{FA}_{15}$	$5.29 \cdot 10^{-15}$	$1.37 \cdot 10^{-16}$
$\overline{\underline{\mathbb{P}}}_{\mathcal{F}}\|\mathcal{H}_0$	$4.95 \cdot 10^{-9}$	$4.36 \cdot 10^{-11}$

The Most Impactful Component (MIC) of $\overline{\underline{\mathbb{P}}}_{\mathcal{F}}|\mathcal{H}_0$ is $\tilde{\underline{\mathsf{P}}}_{\mathrm{FA}_{14}}\tilde{\underline{\mathbb{P}}}_{\mathcal{F}}|\mathrm{FA}_{14} = 4.86 \cdot 10^{-9}$ due to two main reasons: (i) the principal axis of $f_{\underline{\theta}|\mathrm{FA}_{14}}(\theta|\mathrm{FA}_{14})$ is the most aligned with the minor-axis of $\mathcal{B}$ (see Fig. 7), and (ii) the two modes of $f_{\underline{\theta}|\mathrm{FA}_{14}}(\theta|\mathrm{FA}_{14})$ are most far apart from each other along the principal axis leading to the most probability density outside $\mathcal{B}$. Conversely, the principal axes of $f_{\underline{\theta}|\mathrm{FA}_5}(\theta|\mathrm{FA}_5)$ and $f_{\underline{\theta}|\mathrm{FA}_{15}}(\theta|\mathrm{FA}_{15})$ are the most aligned with the major-axis of $\mathcal{B}$ which leads to the Least Impactful Components (LICs): $\tilde{\underline{\mathsf{P}}}_{\mathrm{FA}_5}\tilde{\underline{\mathbb{P}}}_{\mathcal{F}}|\mathrm{FA}_5 = 2.20 \cdot 10^{-15}$ and $\tilde{\underline{\mathsf{P}}}_{\mathrm{FA}_{15}}\tilde{\underline{\mathbb{P}}}_{\mathcal{F}}|\mathrm{FA}_{15} = 5.29 \cdot 10^{-15}$.

A.2 Computation of Level 1 Components of $\mathbb{P}_{\mathcal{F}}|\mathcal{H}_{14}(\mathrm{b}_{14})$

We show the results obtained after computing the components of $\overline{\underline{\mathbb{P}}}_{\mathcal{F}}|\mathcal{H}_{14}(\mathrm{b}_{14}) = \sum_{i=0}^{k=15} \underline{\tilde{\mathcal{M}}}_i|\mathcal{H}_{14}$ for $N_{\mathrm{sim}} = 100$ and a range of values for the size of b_{14} to find the maximum (worst-case size of the outlier). We re-express $\overline{\underline{\mathbb{P}}}_{\mathcal{F}}|\mathcal{H}_{14}(\mathrm{b}_{14})$ in terms of its computed components

$$\overline{\underline{\mathbb{P}}}_{\mathcal{F}}|\mathcal{H}_{14}(\mathrm{b}_{14}) = \mathsf{P}_{\mathrm{MD}_{14}}\tilde{\underline{\mathbb{P}}}_{\mathcal{F}}|\mathrm{MD}_{14} + \tilde{\underline{\mathsf{P}}}_{\mathrm{CI}_{14}}\tilde{\underline{\mathbb{P}}}_{\mathcal{F}}|\mathrm{CI}_{14} + \sum_{i\neq 0,14}^{k=15} \tilde{\underline{\mathsf{P}}}_{\mathrm{WI}_i}\tilde{\underline{\mathbb{P}}}_{\mathcal{F}}|\mathrm{WI}_i. \tag{48}$$

where $\mathsf{P}_{\mathrm{MD}_{14}}$ can be computed exactly. The range of values is chosen between 0 and 2.5 [m] (negative values need not be considered due to the symmetry of the results). The objectives in this sub-section are to compute the components of $\overline{\underline{\mathbb{P}}}_{\mathcal{F}}|\mathcal{H}_{14}(\mathrm{b}_{14})$, determine the maximum $\overline{\underline{\mathbb{P}}}_{\mathcal{F}}|\mathcal{H}_{14}(\mathrm{b}_{14})$, and the corresponding magnitude of b_{14}. As an example, Fig. 8(a) shows the individual probabilities $\mathsf{P}_{\mathrm{MD}_{14}}$ and $\tilde{\underline{\mathbb{P}}}_{\mathcal{F}}|\mathrm{MD}_{14}$ as a function of b_{14}. As the outlier b_{14} increases, the probability density of $f_{\underline{\theta}|\mathrm{MD}_{14}}(\theta|\mathrm{MD}_{14})$ increases in $\mathcal{B}^c$, while $\mathsf{P}_{\mathrm{MD}_{14}}$ decreases. Fig. 8(b) shows that after $\mathsf{P}_{\mathrm{MD}_{14}}\tilde{\underline{\mathbb{P}}}_{\mathcal{F}}|\mathrm{MD}_{14}$ reaches its maximum at $9.42 \cdot 10^{-4}$ for $\mathrm{b}_{14} = 1.70$ [m], the decrease is driven by $\mathsf{P}_{\mathrm{MD}_{14}}$ as its values are significantly smaller than those of $\tilde{\underline{\mathbb{P}}}_{\mathcal{F}}|\mathrm{MD}_{14}$.

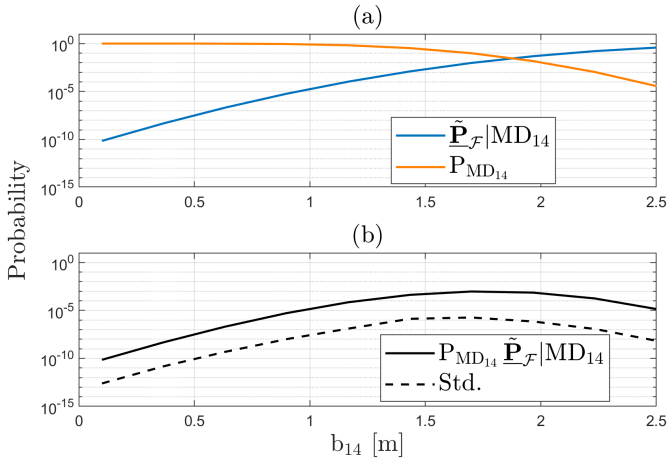

Fig. 8. (a) Individual probabilities $\mathsf{P}_{\mathrm{MD}_{14}}$ and $\tilde{\underline{\mathbb{P}}}_{\mathcal{F}}|\mathrm{MD}_{14}$; (b) Component $\mathsf{P}_{\mathrm{MD}_{14}}\tilde{\underline{\mathbb{P}}}_{\mathcal{F}}|\mathrm{MD}_{14}$ and its simulation standard deviation (Std.) as a function of b_{14}.

The behavior of all of the components from (48) is presented in Fig. 9. For instance, Fig. 9(a) shows that in the case of the event of CI_{14}, as b_{14} increases, the component $\tilde{\underline{\mathsf{P}}}_{\mathrm{CI}_{14}}\tilde{\underline{\mathbb{P}}}_{\mathcal{F}}|\mathrm{CI}_{14}$ exhibits low variation. While b_{14} increases, $\tilde{\underline{\mathsf{P}}}_{\mathrm{CI}_{14}}$ goes toward 1, and $\tilde{\underline{\mathbb{P}}}_{\mathcal{F}}|\mathrm{CI}_{14}$ stabilizes on the order of 10^{-8} for b_{14} larger than 1.2 [m]. An interesting aspect is that $\tilde{\underline{\mathsf{P}}}_{\mathrm{CI}_{14}}\tilde{\underline{\mathbb{P}}}_{\mathcal{F}}|\mathrm{CI}_{14} > \mathsf{P}_{\mathrm{MD}_{14}}\tilde{\underline{\mathbb{P}}}_{\mathcal{F}}|\mathrm{MD}_{14}$ when $\mathrm{b}_{14} < 0.46$ [m] despite $\underline{\mathsf{P}}_{\mathrm{CI}_{14}} < \mathsf{P}_{\mathrm{MD}_{14}}$. Furthermore, this example shows that $\tilde{\underline{\mathsf{P}}}_{\mathrm{CI}_{14}}\tilde{\underline{\mathbb{P}}}_{\mathcal{F}}|\mathrm{CI}_{14}$ is the MIC of $\overline{\underline{\mathbb{P}}}_{\mathcal{F}}|\mathcal{H}_{14}(\mathrm{b}_{14})$ for $\mathrm{b}_{14} < 0.46$ [m], while for $\mathrm{b}_{14} > 0.46$ [m] the MIC is $\mathsf{P}_{\mathrm{MD}_{14}}\tilde{\underline{\mathbb{P}}}_{\mathcal{F}}|\mathrm{MD}_{14}$ until $\tilde{\underline{\mathsf{P}}}_{\mathrm{CI}_{14}}\tilde{\underline{\mathbb{P}}}_{\mathcal{F}}|\mathrm{CI}_{14}$ and $\mathsf{P}_{\mathrm{MD}_{14}}\underline{\mathbb{P}}_{\mathcal{F}}|\mathrm{MD}_{14}$ cross again as $\mathrm{b}_{14} \to \infty$.

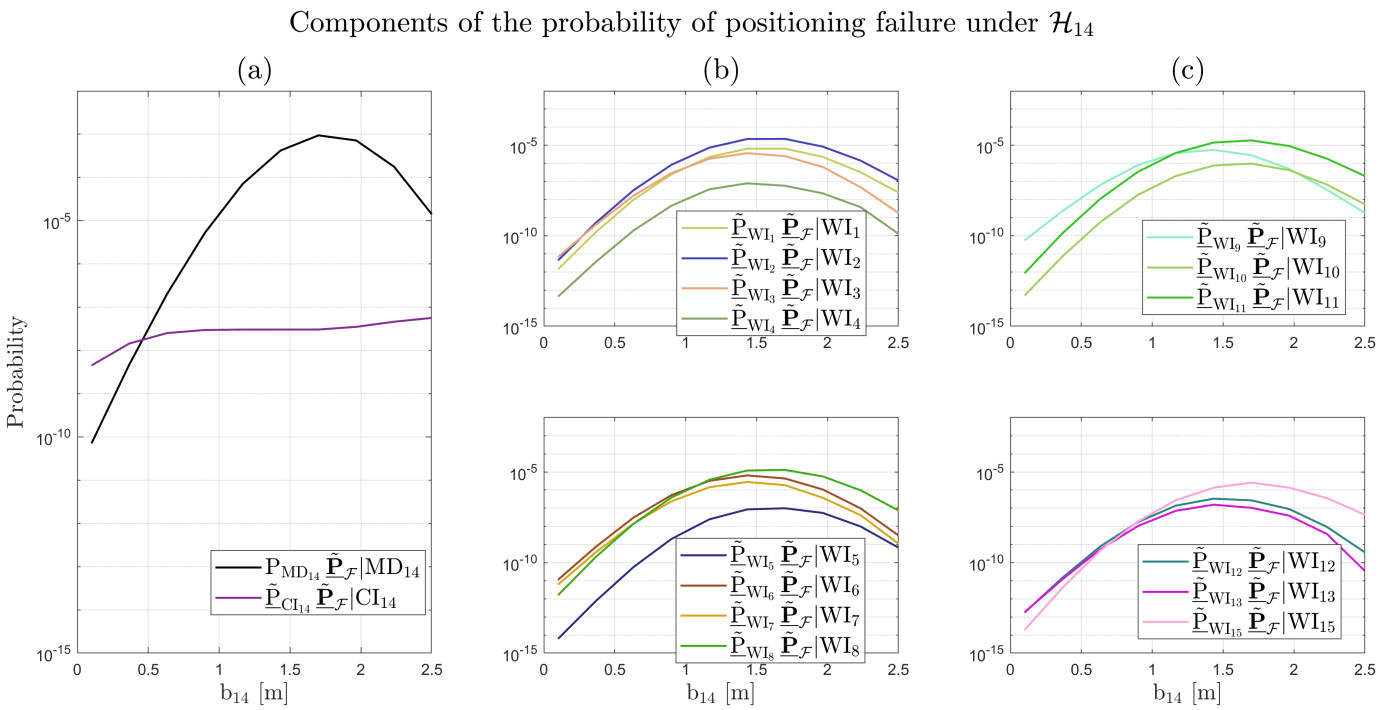

Fig. 9. Level 1 components of $\overline{\underline{\mathbb{P}}}_{\mathcal{F}}|\mathcal{H}_{14}(b_{14})$ for range of outliers $b_{14} \in [0.0,\ 2.5]$ in meters, $P_{FA} = 10^{-3}$ and 10^5 i.i.d. pseudo-random samples generated from IS densities. Curves are mean values obtained based on $N_{sim} = 100$. Mean values of components are: (a) under MD_{14} and CI_{14}; (b) under WI_i corresponding to GPS satellites (for $i \in \{1, ..., 8\}$); (c) under WI_i corresponding to Galileo satellites (for $i \in \{9, 10, 11, 12, 13, 15\}$).

In Fig. 9(b) one can observe that the components under WI_4 and WI_5 have the lowest values (relative to the curves in the top and bottom plots of Fig. 9(b)). The main reasons are: (i) the correlation coefficients between the corresponding w-test statistics $|\,\rho_{w_{14},w_4}\,| = 0.021$ and $|\,\rho_{w_{14},w_5}\,| = 0.088$ are the smallest among all, determining the locations of the main modes of $f_{\overline{\underline{\theta}}|WI_4}(\theta|WI_4)$ and $f_{\overline{\underline{\theta}}|WI_5}(\theta|WI_5)$ to vary slowest as b_{14} increases; (ii) the least probability density of $f_{\overline{\underline{\theta}}|WI_4}(\theta|WI_4)$ and $f_{\overline{\underline{\theta}}|WI_5}(\theta|WI_5)$ outside $\mathcal{B}$. For $b_{14} < 1$ [m] the separation between the components $\tilde{\underline{P}}_{WI_i}\tilde{\underline{\mathbb{P}}}_{\mathcal{F}}|WI_i$ for $i \in \{1, 2, 3, 6, 7, 8\}$ is not significant. This is due to the probability density of the corresponding conditional PDFs not varying significantly outside $\mathcal{B}$, and the separation of the $\tilde{\underline{P}}_{WI_i}$'s not being substantial. On the other hand, the components under WI_1, WI_2, and WI_8 show together a dominant behavior for $b_{14} > 1.5$ [m] due to: (i) the correlation coefficients between the corresponding w-test statistics being the largest, and (ii) the probability density of the corresponding conditional PDFs being the highest in $\mathcal{B}^c$. The same type of reasoning applies for the components in Fig. 9(c).

The Level 1 components in Fig. 9 are then used to compute the function $\overline{\underline{\mathbb{P}}}_{\mathcal{F}}|\mathcal{H}_{14}(b_{14})$ from (48). This function, along with its simulation standard deviation and maximum (gray dot), is shown in Fig. 10. The maximum occurs at $1.02 \cdot 10^{-3}$ for $b_{14} = 1.7$ [m], with its MIC being $P_{MD_{14}}\tilde{\underline{\mathbb{P}}}_{\mathcal{F}}|MD_{14}$. A similar approach is followed for the computation of other Level 1 components $\overline{\underline{\mathbb{P}}}_{\mathcal{F}}|\mathcal{H}_i(b_i)$ for $i \neq \{0, 14\}$.

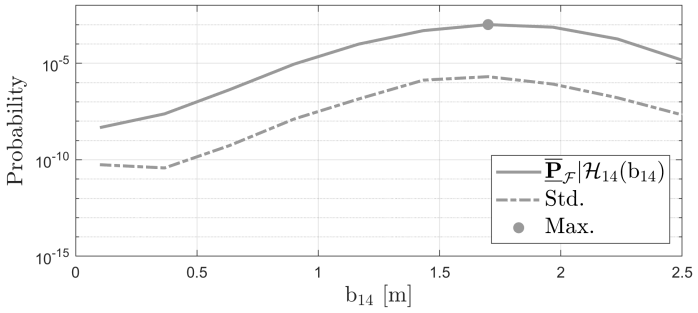

Fig. 10. Obtained $\overline{\underline{\mathbb{P}}}_{\mathcal{F}}|\mathcal{H}_{14}(b_{14})$ as a function of $b_{14} \in [0.0,\ 2.5]$ in meters, its simulaton standard deviation (Std.), and its maximum (max.) at $1.02 \cdot 10^{-3}$.

A.3 Computation of the Level 2 component $\mathbb{P}_{\mathcal{F}}(\mathbf{b})$ for a worst-case scenario

The maximum values of $\overline{\underline{\mathbb{P}}}_{\mathcal{F}}|\mathcal{H}_i(b_i)$ for $i > 0$ have been determined and the results are presented in Table II. The largest three maximum values are given by (in ascending order) $\overline{\underline{\mathbb{P}}}_{\mathcal{F}}|\mathcal{H}_{11}(b_{11})$, $\overline{\underline{\mathbb{P}}}_{\mathcal{F}}|\mathcal{H}_2(b_2)$, $\overline{\underline{\mathbb{P}}}_{\mathcal{F}}|\mathcal{H}_{14}(b_{14})$ as the corresponding PDFs $f_{\overline{\underline{\theta}}}(\theta|\mathcal{H}_i)$, for $i \in \{11, 2, 14\}$, have the largest probability density outside $\mathcal{B}$.

Finally, to compute the worst-case scenario $\mathbb{P}_{\mathcal{F}}(\mathbf{b})$ from (38), some assumptions are needed for the a priori $P(\mathcal{H}_i)'s$ for $i \in \{0, ..., 15\}$. Since alternative hypotheses account for outliers in the pseudoranges at the rover receiver (automated vehicle), it is reasonable to assume that they primarily occur due to different signal reflections caused by the surrounding

TABLE II
OBTAINED $\overline{\mathbb{P}}_{\mathcal{F}}|\mathcal{H}_0$ AND $\overline{\mathbb{P}}_{\mathcal{F}}|\mathcal{H}_i(\mathrm{b}_i)$ FOR $i>0$, THEIR MAXIMUM VALUE, STANDARD DEVIATION (STD.), AND THE SIZE OF THE MODEL OUTLIER WHERE THE MAXIMUM OCCURS.

Comp.	Max. Value	Std.	b_i [m]
$\overline{\mathbb{P}}_{\mathcal{F}}\|\mathcal{H}_0$	$4.95\cdot10^{-9}$	$4.36\cdot10^{-11}$	-
$\overline{\mathbb{P}}_{\mathcal{F}}\|\mathcal{H}_1(\mathrm{b}_1)$	$3.56\cdot10^{-6}$	$1.94\cdot10^{-8}$	5.32
$\overline{\mathbb{P}}_{\mathcal{F}}\|\mathcal{H}_2(\mathrm{b}_2)$	$1.54\cdot10^{-5}$	$7.92\cdot10^{-8}$	3.66
$\overline{\mathbb{P}}_{\mathcal{F}}\|\mathcal{H}_3(\mathrm{b}_3)$	$2.34\cdot10^{-6}$	$1.23\cdot10^{-8}$	2.54
$\overline{\mathbb{P}}_{\mathcal{F}}\|\mathcal{H}_4(\mathrm{b}_4)$	$2.67\cdot10^{-8}$	$2.02\cdot10^{-10}$	1.34
$\overline{\mathbb{P}}_{\mathcal{F}}\|\mathcal{H}_5(\mathrm{b}_5)$	$2.18\cdot10^{-8}$	$2.86\cdot10^{-10}$	1.65
$\overline{\mathbb{P}}_{\mathcal{F}}\|\mathcal{H}_6(\mathrm{b}_6)$	$3.99\cdot10^{-6}$	$2.87\cdot10^{-8}$	1.99
$\overline{\mathbb{P}}_{\mathcal{F}}\|\mathcal{H}_7(\mathrm{b}_7)$	$2.31\cdot10^{-6}$	$9.55\cdot10^{-9}$	1.88
$\overline{\mathbb{P}}_{\mathcal{F}}\|\mathcal{H}_8(\mathrm{b}_8)$	$7.44\cdot10^{-6}$	$2.37\cdot10^{-8}$	1.71
$\overline{\mathbb{P}}_{\mathcal{F}}\|\mathcal{H}_9(\mathrm{b}_9)$	$6.94\cdot10^{-6}$	$5.08\cdot10^{-8}$	1.32
$\overline{\mathbb{P}}_{\mathcal{F}}\|\mathcal{H}_{10}(\mathrm{b}_{10})$	$2.76\cdot10^{-7}$	$8.03\cdot10^{-10}$	2.60
$\overline{\mathbb{P}}_{\mathcal{F}}\|\mathcal{H}_{11}(\mathrm{b}_{11})$	$9.83\cdot10^{-6}$	$3.62\cdot10^{-8}$	1.21
$\overline{\mathbb{P}}_{\mathcal{F}}\|\mathcal{H}_{12}(\mathrm{b}_{12})$	$1.16\cdot10^{-7}$	$5.23\cdot10^{-10}$	3.39
$\overline{\mathbb{P}}_{\mathcal{F}}\|\mathcal{H}_{13}(\mathrm{b}_{13})$	$6.47\cdot10^{-8}$	$3.76\cdot10^{-10}$	1.21
$\overline{\mathbb{P}}_{\mathcal{F}}\|\mathcal{H}_{14}(\mathrm{b}_{14})$	$1.02\cdot10^{-3}$	$2.03\cdot10^{-6}$	1.70
$\overline{\mathbb{P}}_{\mathcal{F}}\|\mathcal{H}_{15}(\mathrm{b}_{15})$	$6.93\cdot10^{-7}$	$5.61\cdot10^{-9}$	1.38

environment (e.g., buildings) [71]. For this analysis, we make three sets of assumptions ranging from more conservative cases to more optimistic ones: (Case 1) $\mathsf{P}(\mathcal{H}_0)=0.8500$ and $\mathsf{P}(\mathcal{H}_i)=10^{-2}$ for $\forall i>0$, (Case 2) $\mathsf{P}(\mathcal{H}_0)=0.9850$ and $\mathsf{P}(\mathcal{H}_i)=10^{-3}$ for $\forall i>0$, (Case 3) $\mathsf{P}(\mathcal{H}_0)=0.9985$ and $\mathsf{P}(\mathcal{H}_i)=10^{-4}$ for $\forall i>0$. The results of the worst-case $\overline{\mathbb{P}}_{\mathcal{F}}(\mathbf{b})$ for these three assumptions are shown in Table III.

TABLE III
MAXIMUM VALUES OF $\overline{\mathbb{P}}_{\mathcal{F}}(\mathbf{b})$ AND THEIR STANDARD DEVIATIONS (STD.).

Cases	$\mathsf{P}(\mathcal{H}_0)$	Max. $\overline{\mathbb{P}}_{\mathcal{F}}(\mathbf{b})$	Std.
1	0.8500	$1.07\cdot10^{-5}$	$2.03\cdot10^{-8}$
2	0.9850	$1.08\cdot10^{-6}$	$2.03\cdot10^{-9}$
3	0.9985	$1.12\cdot10^{-7}$	$2.74\cdot10^{-10}$

In the case of the most conservative assumption ($\mathsf{P}(\mathcal{H}_0)=0.8500$), the maximum $\overline{\mathbb{P}}_{\mathcal{F}}(\mathbf{b})=1.07\cdot10^{-5}\pm2.03\cdot10^{-8}$ can be considered rather large compared to what would be desired from the precision of positioning at the decimeter level (e.g. [7]). However, we emphasize that the present positioning safety analysis is restricted to single-epoch (snapshot) GNSS-only positioning and it does not consider a sensor suite for positioning.

A.4 Verification of the results

Using the direct simulation approach based on the standard MC, as described in the appendix of [72], we verify the results of Tables II and III using 10^6 i.i.d. pseudo-random samples and $N_{\text{sim}}=100$. The results are presented below in Tables IV and V and they agree with the ones from Tables III and IV (the relative differences are $<20\%$). A dash '$-$' in Table IV indicates that the target value is around or below 10^{-8} and it could not be computed reliably with 10^6 i.i.d. pseudo-random samples and $N_{\text{sim}}=100$. Therefore, they are also not taken into account in the generation of Table V. To generate these results for verification, we have used computational resources from the Delft High Performance Computing Center (DHPC) [73].

TABLE IV
VERIFICATION OF RESULTS IN TABLE VI BASED ON STANDARD MC APPROACH IN APPENDIX OF [72].

Comp.	Max. Value	Std.	b_i [m]
$\overline{\mathbb{P}}_{\mathcal{F}}\|\mathcal{H}_0$	-	-	-
$\overline{\mathbb{P}}_{\mathcal{F}}\|\mathcal{H}_1(\mathrm{b}_1)$	$3.75\cdot10^{-6}$	$2.00\cdot10^{-7}$	5.32
$\overline{\mathbb{P}}_{\mathcal{F}}\|\mathcal{H}_2(\mathrm{b}_2)$	$1.54\cdot10^{-5}$	$4.21\cdot10^{-7}$	3.66
$\overline{\mathbb{P}}_{\mathcal{F}}\|\mathcal{H}_3(\mathrm{b}_3)$	$2.27\cdot10^{-6}$	$1.48\cdot10^{-7}$	2.54
$\overline{\mathbb{P}}_{\mathcal{F}}\|\mathcal{H}_4(\mathrm{b}_4)$	-	-	-
$\overline{\mathbb{P}}_{\mathcal{F}}\|\mathcal{H}_5(\mathrm{b}_5)$	-	-	-
$\overline{\mathbb{P}}_{\mathcal{F}}\|\mathcal{H}_6(\mathrm{b}_6)$	$4.60\cdot10^{-6}$	$2.20\cdot10^{-7}$	1.99
$\overline{\mathbb{P}}_{\mathcal{F}}\|\mathcal{H}_7(\mathrm{b}_7)$	$2.35\cdot10^{-6}$	$1.61\cdot10^{-7}$	1.88
$\overline{\mathbb{P}}_{\mathcal{F}}\|\mathcal{H}_8(\mathrm{b}_8)$	$7.78\cdot10^{-6}$	$2.94\cdot10^{-7}$	1.71
$\overline{\mathbb{P}}_{\mathcal{F}}\|\mathcal{H}_9(\mathrm{b}_9)$	$6.69\cdot10^{-6}$	$2.50\cdot10^{-7}$	1.32
$\overline{\mathbb{P}}_{\mathcal{F}}\|\mathcal{H}_{10}(\mathrm{b}_{10})$	$3.40\cdot10^{-7}$	$5.72\cdot10^{-8}$	2.60
$\overline{\mathbb{P}}_{\mathcal{F}}\|\mathcal{H}_{11}(\mathrm{b}_{11})$	$1.01\cdot10^{-5}$	$3.48\cdot10^{-7}$	1.21
$\overline{\mathbb{P}}_{\mathcal{F}}\|\mathcal{H}_{12}(\mathrm{b}_{12})$	$1.20\cdot10^{-7}$	$3.27\cdot10^{-8}$	3.39
$\overline{\mathbb{P}}_{\mathcal{F}}\|\mathcal{H}_{13}(\mathrm{b}_{13})$	-	-	-
$\overline{\mathbb{P}}_{\mathcal{F}}\|\mathcal{H}_{14}(\mathrm{b}_{14})$	$1.02\cdot10^{-3}$	$3.26\cdot10^{-6}$	1.70
$\overline{\mathbb{P}}_{\mathcal{F}}\|\mathcal{H}_{15}(\mathrm{b}_{15})$	$7.80\cdot10^{-7}$	$9.27\cdot10^{-8}$	1.38

TABLE V
VERIFICATION OF RESULTS IN TABLE III USING THE VALUES FROM TABLE IV.

Cases	$\mathsf{P}(\mathcal{H}_0)$	Max. $\overline{\mathbb{P}}_{\mathcal{F}}(\mathbf{b})$	Std.
1	0.8500	$1.07\cdot10^{-5}$	$3.35\cdot10^{-8}$
2	0.9850	$1.07\cdot10^{-6}$	$3.35\cdot10^{-9}$
3	0.9985	$1.07\cdot10^{-7}$	$3.35\cdot10^{-10}$

B. Probability of positioning failure for varying vehicle and safety-region orientation

Although vehicles change their orientation as they move—for example, when making U-turns, exiting highways, or turning left or right—over a short time frame (e.g., a few minutes), we can assume that the receiver-satellite geometry depicted in Fig. 5 remains constant because GNSS satellites orbit Earth at altitudes around 20.000 km. This assumption allows us to focus our analysis on the vehicle's changing orientation. Therefore, we modify the safety region from (45) to incorporate dependence on the orientation angle ϕ, measured clockwise relative to the vertical axis,

$$\mathcal{B}_\phi=\{\theta\in\mathbb{R}^2 \mid ||\theta-\theta_{\text{true}}||^2_{\mathrm{Q}_{\mathcal{B}_\phi}}\leq 1\}, \tag{49}$$

where $\mathrm{Q}^{-1}_{\mathcal{B}_\phi}$ now depends on ϕ and $\phi\in[0^\circ,\ 180^\circ]$. The maximum $\overline{\mathbb{P}}_{\mathcal{F}}(\mathbf{b})$ is computed as *a function* of ϕ from its components: $\overline{\mathbb{P}}_{\mathcal{F}}|\mathcal{H}_0$ and $\max\limits_{\mathrm{b}_1,\ldots,\mathrm{b}_k}\sum_{i=1}^{15}\overline{\mathbb{P}}_{\mathcal{F}}|\mathcal{H}_i(\mathrm{b}_i)$. Fig. 11(a) illustrates the variations of $\overline{\mathbb{P}}_{\mathcal{F}}|\mathcal{H}_0$ as a function of ϕ. As ϕ

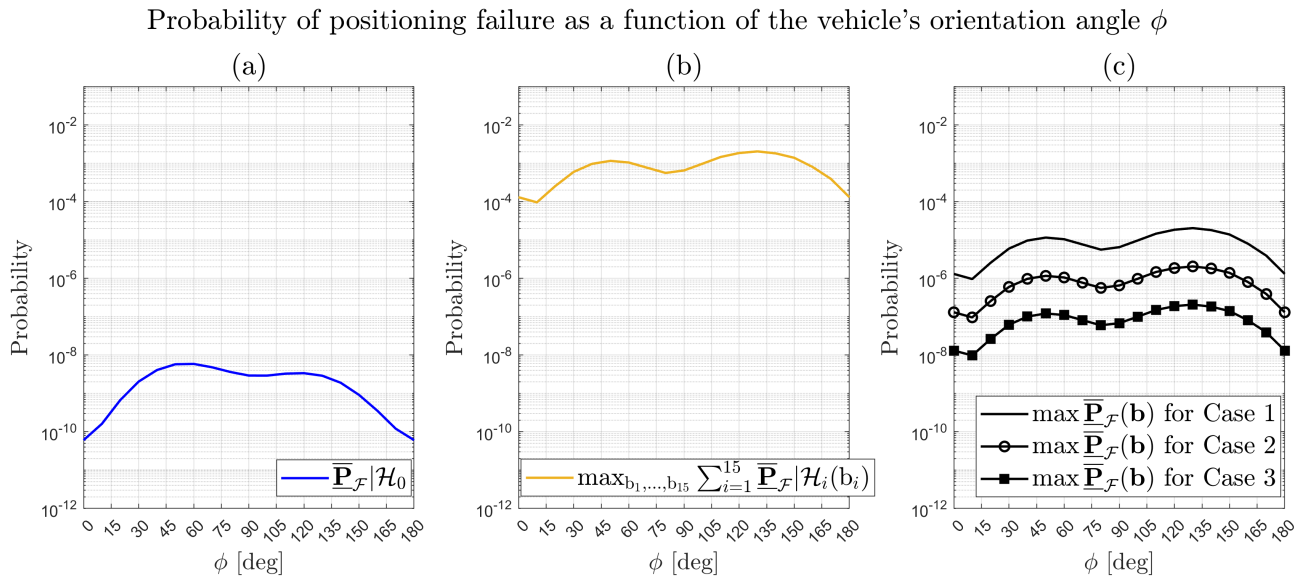

Fig. 11. (a) Computed $\overline{\mathbb{P}}_{\mathcal{F}}|\mathcal{H}_0$ over the angles ϕ with $N_{\text{sim}} = 50$; (b) Computed $\max\limits_{b_1,\ldots,b_k} \sum_{i=1}^{k} \overline{\mathbb{P}}_{\mathcal{F}}|\mathcal{H}_i(b_i)$ over the angles ϕ with $N_{\text{sim}} = 50$; (c) Computed maximum total probability of positioning failure $\overline{\mathbb{P}}_{\mathcal{F}}(\mathbf{b})$ over the angles ϕ for the three cases: (i) Case 1 when the a-priori $\mathsf{P}(\mathcal{H}_0) = 0.8500$ and $\mathsf{P}(\mathcal{H}_i) = 10^{-2}$ for $i \in \{1, \ldots, 15\}$, (ii) Case 2 when the a-priori $\mathsf{P}(\mathcal{H}_0) = 0.9850$ and $\mathsf{P}(\mathcal{H}_i) = 10^{-3}$ for $i \in \{1, \ldots, 15\}$, and (iii) Case 3 when the a-priori $\mathsf{P}(\mathcal{H}_0) = 0.9985$ and $\mathsf{P}(\mathcal{H}_i) = 10^{-4}$ for $i \in \{1, \ldots, 15\}$.

approaches $60°$, the components of $f_{\overline{\theta}}(\theta|\mathcal{H}_0)$ that are less aligned with $\mathcal{B}_\phi$ contribute the most (e.g., see $f_{\overline{\theta}|\text{FA}_6}(\theta|\text{FA}_6)$, $f_{\overline{\theta}|\text{FA}_{14}}(\theta|\text{FA}_{14})$ from Fig. 7), reaching a global maximum of $5.87 \cdot 10^{-9}$ at $\phi = 60°$. For $\phi > 60°$, the values of $\overline{\mathbb{P}}_{\mathcal{F}}|\mathcal{H}_0$ decrease until $\phi = 100°$, after which they begin to rise again, reaching a local maximum of $3.37 \cdot 10^{-9}$ at $\phi = 120°$ due to $f_{\overline{\theta}|\text{FA}_5}(\theta|\text{FA}_5)$, $f_{\overline{\theta}|\text{FA}_{10}}(\theta|\text{FA}_{10})$, and $f_{\overline{\theta}|\text{FA}_{15}}(\theta|\text{FA}_{15})$ having most of their probability density outside $\mathcal{B}_\phi$. A similar reasoning can be applied to the behaviour of $\max\limits_{b_1,\ldots,b_k} \sum_{i=1}^{15} \overline{\mathbb{P}}_{\mathcal{F}}|\mathcal{H}_i(b_i)$ in Fig. 11(b).

The results from Fig. 11(a) and 11(b) are combined with the assumptions made on the a-priori probabilities $\mathsf{P}(\mathcal{H}_0)$ and $\mathsf{P}(\mathcal{H}_i)$ for $i > 0$, as discussed previously, to obtain the results from Fig. 11(c). In the most conservative case (Case 1), the maximum $\overline{\mathbb{P}}_{\mathcal{F}}(\mathbf{b})$ at $\phi = 130°$ is $2.04 \cdot 10^{-5}$ while for the most optimistic (Case 3) is $2.07 \cdot 10^{-7}$ (see Table VI). Considering this is a snapshot positioning scenario for an automated vehicle with decimeter-level accuracy and a horizontal positioning precision of approximately 0.5 meters (95% circular probability radius), while accounting for one-dimensional outliers in the observables, the result in Case 1 is relatively large.

This type of results helps determine whether the target requirements or guidelines for positioning safety are met at a particular time instant. This assessment is based on the assumed functional and stochastic models in (39), the receiver-satellite geometry in Fig. 5, the statistical hypothesis testing procedure in (40)-(42), and the safety-region $\mathcal{B}_\phi$ defined in (49).

If the requirements or guidelines are not met, adjustments

TABLE VI
MAXIMUM VALUES OF $\overline{\mathbb{P}}_{\mathcal{F}}(\mathbf{b})$ AT THE WORST-ORIENTATION OF THE VEHICLE W.R.T. THE SATELLITE GEOMETRY FROM FIG. 5.

Cases	$\mathsf{P}(\mathcal{H}_0)$	Max. $\overline{\mathbb{P}}_{\mathcal{F}}(\mathbf{b})$ at $\phi = 130°$	Std.
1	0.8500	$2.04 \cdot 10^{-5}$	$4.52 \cdot 10^{-7}$
2	0.9850	$2.04 \cdot 10^{-6}$	$4.52 \cdot 10^{-8}$
3	0.9985	$2.07 \cdot 10^{-7}$	$4.52 \cdot 10^{-9}$

may be needed in various aspects, such as the measurement setup (including functional and stochastic models), the definition of the safety region, or the combined approach for parameter estimation and statistical hypothesis testing. For example, recent theoretical advancements show how tailored statistical hypothesis testing can improve the performance of DIA-estimators [41].

C. Computational resources

To provide context regarding the computational resources used to carry-out the positioning safety analyses based on the proposed method, we detail the used hardware and software. The computations were performed on a laptop Dell Latitude 7440 equipped with a 13th Gen Intel Core i7 processor featuring 10 physical cores and 16 GB RAM. The operating system is Windows 10 Enterprise and the programming language is MATLAB 2024a with the Parallel Computing Toolbox. The analyses leveraged 8 physical cores of the processor through MATLAB's parallel computing capabilities.

For example, the computation time to generate the results from Table I (components of $\overline{\mathbb{P}}_{\mathcal{F}}|\mathcal{H}_0$) with $\tilde{N}_i = 10^5$ (for $i \geq 0$) i.i.d. pseudo-random samples generated from the IS densities and $N_{\text{sim}} = 100$ for the simulation uncertainty

quantification, was ≈ 5 minutes. To obtain the results from Fig. 9 (components of $\overline{\mathbb{P}}_{\mathcal{F}}|\mathcal{H}_{14}(\mathrm{b}_{14})$ evaluated at 10 values of b_{14}), with $\check{N}_i = 10^5$ (for $i \geq 0$) i.i.d. pseudo-random samples generate from the IS densities and $N_{\text{sim}} = 100$, was ≈ 50 minutes. For the other alternative hypotheses, the computations times ranged between ≈ 50 minutes and ≈ 150 minutes. Note that these computation times can be improved if more physical cores are available and by reducing the number of independent simulation repetitions N_{sim} (e.g., to 50 [53]). They also depend on the chosen programming language, code implementation and the configuration parameters of the CE method. To generate the results from Table IV and Fig. 11 we have used computational resources from Delft High Performance Computing Centre (DHPC) [73].

Limitations and potential improvements of the proposed method

We now turn our attention to limitations of the proposed method, emphasizing those that, in our opinion, are particularly relevant to address in future work.

- Dimensionality of $\mathrm{b}_i \in \mathbb{R}^{q_i}$: The computation of a $\overline{\mathbb{P}}_{\mathcal{F}}|\mathcal{H}_i(\mathrm{b}_i)$, for $i > 0$, requires assumptions on the values of $\mathrm{b}_i \in \mathbb{R}^{q_i}$. Currently, the maximum $\overline{\mathbb{P}}_{\mathcal{F}}|\mathcal{H}_i(\mathrm{b}_i)$ is found by defining a range for $\mathrm{b}_i \in \mathbb{R}^{q_i}$, when $q_i = 1$, and then perform the computations (e.g., Fig. 9). This approach can be computationally too expensive, especially when $q_i > 1$, as it would require searches over q_i-dimensional grids. Therefore, a more efficient approach to find the maximum $\underline{\mathbb{P}}_{\mathcal{F}}|\mathcal{H}_i(\mathrm{b}_i)$ is sought.
- Integration regions $\mathcal{B}^c \cap \mathcal{P}_i$: The expected values in (17) are integrals over the regions resulting from $\mathcal{B}^c \cap \mathcal{P}_i$ for $i \in \{0, ..., k\}$. A characterization of these regions by determining, a priori, their number and potentially their relative 'distance' (w.r.t. some metric), could offer insights for better choices of families of PDFs for the IS densities. In this context, choosing the parametric family of Gaussian PDFs for the IS density may not always be appropriate, especially if the dimension of the misclosure vector $\underline{\mathrm{t}} \in \mathbb{R}^r$ becomes large (e.g., > 40). Once this type of characterization is done, several approaches can be tried with respect to the choice of the parametric family for IS densities [55]–[57].
- Initialization of the CE method: Currently, the distributional parameters of IS densities are found by solving (36) using the (multilevel) CE method, as described in [51] (page 73). In this approach, the initialization parameters of the CE method, such as (i) initial IS densities to start the CE method and (ii) number of i.i.d. pseudo-random samples to be used $\check{N}_{\text{CE}}$, are chosen empirically. To overcome some of these shortcomings, a Fully Adaptive Cross-Entropy (FACE) method is proposed in Chapter 5 of [51] .

It is also important to mention that improvements of the CE method, especially for high-dimensional problems, have been recently proposed in [74], [75]. Such studies and developments could also bring benefits in the context of our proposed method (i.e., solving (36)).

V. Summary and Conclusions

The study of the event of positioning failure $\mathcal{F} = \underline{\mathrm{x}} \in \mathcal{B}^c$ [6], through computing its probability $\mathbb{P}_{\mathcal{F}}(\mathbf{b})$, is of importance for a wide range of safety-critical applications in automotive, aviation, rail, and maritime domains. In this contribution, we have proposed a method to compute the probability of positioning failure and its conditional components, while accounting for the dependence between parameter estimation and statistical hypothesis testing. In addition, our proposed method allows positioning safety when the dimension of the position vector is larger than one (i.e., $n > 1$). The method has been developed based on principles and techniques from rare event simulation, specifically Importance Sampling and the Cross-Entropy method [37], [38]. Three limitations of the proposed method, along with potential improvements, have also been discussed: (i) handling the increase in the computation time due to the dimensionality of the model misspecification $\mathrm{b}_i \in \mathbb{R}^{q_i}$ for $i > 0$, (ii) accounting for the characteristics of the integration regions $\mathcal{B}^c \cap \mathcal{P}_i$ in the choices of the family of PDFs for the IS densities (other than the Gaussian PDFs), and (iii) the initialization strategy of the CE method which currently is empirical. These limitations can be alleviated by recent advances in the CE method (e.g., [55]–[57], [74], [75]) and by adaptive versions of it [51]. These topics represent areas to explore in future work.

The computation and analysis of $\mathbb{P}_{\mathcal{F}}(\mathbf{b})$ is aimed at the design stage of positioning algorithms, where decisions are to be made about (i) measurement models, (ii) parameter estimation methods for the position vector, (iii) statistical hypothesis testing procedures to accommodate for model misspecifications (e.g., outliers or faults in measurements), and (iv) positioning scenarios for vehicles, among other factors. This approach aligns with the principles of scenario-based safety assessment framework which is used or proposed for studies of automated and autonomous vehicles [11]–[13]. As an example, we have applied the proposed method to perform a positioning safety analysis, at a single epoch, for an automated vehicle in the context of decimeter-level precision GNSS positioning. The method enabled an extensive analysis of a worst-case scenario with the objective of finding the maximum $\underline{\mathbb{P}}_{\mathcal{F}}(\mathbf{b})$. Such analyses can be used to decide whether positioning safety targets or requirements are met. Although the chosen positioning scenario was centered in the automotive domain, the method for computing the probability of positioning failure and its analysis are also applicable to other safety-critical fields such as civil aviation, shipping, and rail. Further improvements of the proposed method can be made based on the existing literature and recent advances in the CE method, extending the range of scenarios for positioning safety analyses and development of positioning algorithms. Moreover, since the dependence between parameter estimation and statistical hypothesis testing has been acknowledged across various disciplines such as mathematical statistics, biometrics, econometrics, and signal processing [21]–[26], the principles of the distributional

theory for the DIA method and the proposed method of the present contribution may also be applicable there, particularly in the context of linear(ized) functional models.

ACKNOWLEDGMENTS

This research was funded by the Dutch Research Council (NWO) under Grant 18305 I-GNSS Positioning for Assisted and Automated Driving. We appreciate the support of colleague Chengyu Yin of Department of Geoscience and Remote Sensing (Delft University of Technology) for providing the functional and stochastic models for the GNSS scenario. We extend our gratitude to Hayden Dorahy of u-blox AG, Dr. Zoltán Perkó of Department of Radiation Science and Technology at Faculty of Applied Sciences (Delft University of Technology), and Dr. Oswaldo Morales Napole of Department of Hydraulic Structures and Flood Risk at Faculty of Civil Engineering and Geosciences (Delft University of Technology). The insightful discussions were beneficial in the development of the method presented in this paper.

REFERENCES

[1] P. J. G. Teunissen and O. Montenbruck, Eds., Handbook of Global Navigation Satellite Systems. Springer, 2017.

[2] J. C. J. Koelemeij, et al., "A hybrid optical-wireless network for decimetre-level terrestrial positioning," *Nature*, vol. 611, no. 7936, pp. 473–478, Nov. 2022.

[3] N. Nadarajah, P. J. G. Teunissen, and N. Raziq, "Instantaneous GPS-Galileo Attitude Determination: Single-Frequency Performance in Satellite-Deprived Environments," *IEEE Trans. Veh. Technol.*, vol. 62, nb. 7, pp. 2963–2976, 2013.

[4] B. C. Vani et al., "A Novel Approach to Improve GNSS Precise Point Positioning During Strong Ionospheric Scintillation: Theory and Demonstration," *IEEE Trans. Veh. Technol.*, vol. 68, nb. 5, pp. 4391–4403, 2021.

[5] V. G. Juan et al., "Asynchronous Sensor Fusion of GPS, IMU and CAN-Based Odometry for Heavy-Duty Vehicles," *IEEE Trans. Veh. Technol.*, vol. 70, nb. 9, pp. 8617–8626, 2021.

[6] RTCA-Special Committee 159, "Minimum Operational Performance Standards (MOPS) for Global Positioning System/Satellite-Based Augmentation System Airborne Equipment," DO-229F, Radio Technical Commission for Aeronautics, pp. 15, 2020.

[7] T. G. R. Reid, et al., "Localization Requirements for Autonomous Vehicles," *SAE Int. J. Connect. Autom. Veh.*, 2019.

[8] K. Jin, et al., "An approach to constructing effective training data for a classification model to evaluate the reliability of a passive safety system," *Reliab. Eng. Syst. Saf.*, vol. 222, pp. 1–10, 2022.

[9] V. Chabridon, et al., "Evaluation of failure probability under parameter epistemic uncertainty: Application to aerospace system reliability assessment," *Aerosp. Sci. Technol.*, vol. 69, pp. 526–537, 2017.

[10] M. Shinozuka, "Basic analysis of structural safety," *J. Struct. Eng.*, vol. 109, no. 3, pp. 721–740, 1983.

[11] S. Riedmaier et al., "Survey on Scenario-Based Safety Assessment of Automated Vehicles," *IEEE Access*, vol. 8, pp. 87456–87477, 2020.

[12] U.N.E.C.E., "New Assessment/Test Method for Automated Driving (NATM) Guidelines for Validating Automated Driving Systems (ADS)," United Nations Economic Commission for Europe - Inland Transport Committee, Report, 2023.

[13] E. de Gelder et al., "TNO Street Wise: Scenario-Based Safety Assessment of Automated Driving Systems," Netherlands Organisation for Applied Scientific Research (TNO), White Paper, 2024.

[14] P. J. G. Teunissen, "An integrity and quality control procedure for use in multi-sensor integration," *ION GPS*, pp. 513–522, 1990.

[15] I. Gillissen and I. A. Elema, "Test results of DIA: A real-time adaptive integrity monitoring procedure, used in an integrated navigation system," *Int. Hydro. Rev.*, vol. 73, nb. 1, pp. 75—103, 1996.

[16] L. Yang, Y. Li, and C. Rizos, "An enhanced MEMS-INS/GNSS integrated system with fault detection and exclusion capability for land vehicle navigation in urban areas," *GPS Solut.*, vol. 18, no. 4, pp. 593–603, 2013.

[17] J. Liu, G. Guo, and R. Zhang., "Residual-Based Fault Detection and Exclusion With Enhanced Localization Integrity," *IEEE Trans. Veh. Technol.*, vol. 72, nb. 5, pp. 5798–5808, 2023.

[18] P. J. G. Teunissen, "Distributional theory for the DIA method," *J. Geod.*, vol. 92, no. 1, pp. 59–80, 2018.

[19] S. Zaminpardaz, P. J. G. Teunissen, and C. C. J. M. Tiberius, "Risking to underestimate the integrity risk," *GPS Solut.*, vol. 23, no. 29, pp. 1–16, 2019.

[20] S. Zaminpardaz and P. J. G. Teunissen, "On the computation of confidence regions and error ellipses: A critical appraisal," *J. Geod.*, vol. 96, no. 10, pp. 1–18, 2022.

[21] T. A. Bancroft, "On Biases in Estimation Due to the Use of Preliminary Tests of Significance," *Ann. Math. Stat.*, vol. 15, no. 2, pp. 190–204, 1944.

[22] S. Sarkadi, "Estimation after selection," *Stud. Sci. Math. Hungarica*, pp. 341–350, 1967.

[23] N. L. Hjort and G. Claeskens, "Frequentist Model Average Estimators," *J. Am. Stat. Assoc.*, vol. 98, no. 464, pp. 879–899, 2003.

[24] S. T. Buckland, K. P. Burnham, and N. H. Augustin, "Model Selection: An Integral Part of Inference," *Biom.*, vol. 53, nr. 2, pp. 603–618, 1997.

[25] H. Leeb and B. M. Pötscher, "The Finite-Sample Distribution of Post-Model-Selection Estimators and Uniform versus Nonuniform Approximations," *Econom. Theor.*, vol. 19, nr. 1, pp. 100–142, 2003.

[26] T. Routtenberg and L. Tong, "Estimation After Parameter Selection: Performance Analysis and Estimation Methods," *IEEE Trans. Signal Process.*, vol. 64, no. 20, pp. 5268–5281, 2016.

[27] J. Blanch, et al., "Baseline Advanced RAIM User Algorithm and Possible Improvements," *IEEE Aerosp. Electr. Syst.*, vol. 51, nb. 1, pp. 713–732, 2015.

[28] Working Group C, "Advanced RAIM Technical Subgroup Reference Airborne Algorithm Description Document," Version 3.1, 2019.

[29] P. Zhao et al., "A New Method to Bound the Integrity Risk for Residual-Based ARAIM," *IEEE Aerosp. Electron. Syst.*, vol. 57, no. 2, pp. 1378–1385, 2020.

[30] G. Huang et al., "Bayesian fault-tolerant protection level for multi-constellation navigation from integrity perspective," *Aerosp. Sci. Technol.*, vol. 130, no. 107954, 2022.

[31] S. Wang et al., "Bayesian upper bound on GNSS posterior integrity risk," *IEEE Trans. Aerosp. Electron. Syst.*, vol. 60, no. 6, pp. 7945–7961, Dec. 2024.

[32] L. Li et al., "GNSS integrity risk evaluation in the position domain based on the generalized Pareto distribution," *Meas. Sci. Technol.*, vol. 34, no. 8, pp. 1–11, 2023.

[33] N. Zhu et al., "GNSS Position Integrity in Urban Environments: A Review of Literature," *IEEE Trans. Intell. Transp. Syst.*, vol. 19, no. 9, pp. 2762–2778, 2018.

[34] G. Gottschalg et al., "Integrity Concept for Sensor Fusion Algorithms used in a Prototype Vehicle for Automated Driving," *European Navigation Conference*, pp. 1–10, 2020.

[35] H. Jing et al., "Integrity Monitoring of GNSS/INS Based Positioning Systems for Autonomous Vehicles: State-of-the-Art and Open Challenges," *IEEE Trans. Intell. Transp. Syst.*, vol. 23, no. 9, pp. 14166–14187, 2022.

[36] D. P. Kroese, T. Taimre, and Z. I. Botev, Eds., *Handbook of Monte Carlo Methods*, Wiley Ser. Prob Stat., 2011.

[37] H. Kahn and A. W. Marshall, "Methods of Reducing Sample Size in Monte Carlo Computations," *J. Oper. Res. Soc. Am.*, vol. 1, no. 5, pp. 263–278, 1953.

[38] R. Y. Rubinstein, "The Cross-Entropy Method for Combinatorial and Continuous Optimization," *Methodol. Comput. Appl. Prob.*, vol. 1, pp. 127–190, 1999.

[39] P. J. G. Teunissen, "Batch and Recursive Model Validation," in Springer Handbook of Global Navigation Satellite Systems, P. J. G. Teunissen and O. Montenbruck, Eds. Springer, pp. 687–720, 2017.

[40] S. Zaminpardaz and P. J. G. Teunissen, "Detection-only versus detection and identification of model misspecifications," *J. Geod.*, vol. 97, no. 55, pp. 1–19, 2023.

[41] P. J. G. Teunissen, "On the Optimality of DIA-Estimators: Theory and Applications," *J. Geod.*, vol. 98, no. 43, pp. 1–26, 2024.

[42] D. Odijk, "Positioning Model," in Springer Handbook of Global Navigation Satellite Systems, P. J. G. Teunissen and O. Montenbruck, Eds. Springer, p. 617, 2017.

[43] D. P. Kroese and R. Y. Rubinstein, "The Transform Likelihood Ratio Method for Rare Event Simulation with Heavy Tails," *Queueing Syst.*, vol. 46, no. 3/4, pp. 317–351, 2004.

[44] R. V. Rubinstein and D. P. Kroese, Simulation and the Monte Carlo Method. Wiley Ser. Prob. Stat., 2008.

[45] I. Papaioannou, C. Papadimitriou, and D. Straub, "Sequential Importance Sampling for Structural Reliability Analysis," *Struct. Saf.*, vol. 62, pp. 66–75, 2016.
[46] B. J. Garrick, et al., Reliability analysis of nuclear power plant protective systems (Research and Development Report). Holmes and Narver Inc. Nuclear Division, 1967.
[47] M. Mitici and H. A. P. Blom, "Mathematical Models for Air Traffic Conflict and Collision Probability Estimation," *IEEE Trans. Intell. Transp. Syst.*, vol. 20, no. 3, pp. 1052–1068, 2019.
[48] G. Biondini, "An Introduction to Rare Event Simulation and Importance Sampling," in Handbook of Statistics, Elsevier B.V, V. Govindaraju, V. V. Raghavan, and C. R. Rao, Eds., pp. 29–68, 2015.
[49] R. Y. Rubinstein, "Optimization of computer simulation models with rare events," *Eur. J. Oper. Res.*, vol. 99, no. 1, pp. 89–112, 1997.
[50] S. Kullback and R. A. Leibler, "On Information and sufficiency," *Ann. Math. Stat.*, vol. 22, no. 1, pp. 79–86, 1951.
[51] R. V. Rubinstein and D. P. Kroese, The Cross-Entropy Method: A Unified Approach to Combinatorial Optimization, Monte-Carlo Simulation, and Machine Learning. Springer Ser. Inf. Sci. Stat., 2004.
[52] P. T. de Boer, et al., "A Tutorial on the Cross-Entropy Method," *Ann. Op. Res.*, vol.134, pp. 19–67, 2005.
[53] J. Morio and M. Balesdent, Estimation of Rare Event Probabilities in Complex Aerospace and Other Systems - A Practical Approach. Elsevier B.V, 2016.
[54] M. El Masri, J. Morio, and F. Simatos, "Improvement of the cross-entropy method in high dimension for failure probability estimation through a one-dimensional projection without gradient estimation," *Reliab. Eng. Syst. Saf.*, vol. 216, pp. 1–10, 2021.
[55] S. Geyer, I. Papaioannou, and D. Straub, "Cross entropy-based adaptive importance sampling using Gaussian densities revisited," *Struct. Saf.*, vol. 76, pp. 15–27, 2019.
[56] N. Kurtz and J. Song, "Cross-entropy-based adaptive importance sampling using Gaussian mixture," *Struct. Saf.*, vol. 42, pp. 35–44, 2013.
[57] Z. Wang and J. Song, "Cross-entropy-based adaptive importance sampling using von Mises-Fisher mixture for high dimensional reliability analysis," *Struct. Saf.*, vol. 59, pp. 42–52, 2016.
[58] G. Weber, et al., "Networked transport of RTCM via internet protocol (Ntrip) - IP - streaming for real-time GNSS applications," *ION GNSS*, pp. 2243–2247, 2005.
[59] A. Kealy and T. Moore, "Land-based Applications of GNSS," in Springer Handbook of Global Navigation Satellite Systems, P. J. G. Teunissen and O. Montenbruck, Eds. Springer, pp. 842–856, 2017.
[60] D. Odijk and L. Wanninger, "Differential Positioning," in Springer Handbook of Global Navigation Satellite Systems, P. J. G. Teunissen and O. Montenbruck, Eds. Springer, pp. 687–720, 2017.
[61] D. Odijk, Fast precise GPS positioning in the presence of ionospheric delays (PhD Thesis). Delft University of Technology, 2002.
[62] D. Odijk, "Positioning Model," in Springer Handbook of Global Navigation Satellite Systems, P. J. G. Teunissen and O. Montenbruck, Eds. Springer, pp. 623–630, 2017.
[63] H. J. Eueler and C. C. Goad, "On optimal filtering of GPS dual frequency observations without using orbit information," *Bull. Geod.*, vol. 65, no. 2, pp. 130–143, 1991.
[64] A. Hauschild, "Combination of Observations," in Handbook of Global Navigation Satellite Systems, P. J. G. Teunissen and O. Montenbruck, Eds. Springer, pp. 594–596, 2017.
[65] P. J. G. Teunissen, "Nonlinear least squares," *Manuscr. Geod.*, vol. 15, no. 3, pp. 137–150, 1990.
[66] W. Baarda, "A testing procedure for use in geodetic networks," *Netherlands Geodetic Commission, Publ Geod*, vol. 2, nr. 5, pp. 1–97, 1968a.
[67] J. J. Kok, On data snooping and multiple outlier testing. US Department of Commerce, National Oceanic and Atmospheric Administration, National Ocean Service, Charting and Geodetic Services, 1984.
[68] W. Baarda, "Statstical concepts in geodesy," *Netherlands Geodetic Commission, Publ. Geod.*, vol. 2, nr. 4, pp. 1–74, 1967.
[69] Y. Feng, C. Wang, and C. Karl, "Determination of Required Positioning Integrity Parameters for Design of Vehicle Safety Applications,", *ION GNSS*, pp. 129–141, 2018.
[70] O. N. Kigotho and J. H. Rife, "Comparison of Rectangular and Elliptical Alert Limits for Lane-Keeping Applications,", *ION GNSS*, pp. 93–104, 2021.
[71] Ç. Tanil, et al., "Optimal INS/GNSS Coupling for Autonomous Car Positioning Integrity," *ION GNSS*, pp. 3123–3140, 2019.
[72] S. Ciuban, P. J. G. Teunissen, and C. C. J. M. Tiberius, "GNSS Positioning Safety: Probability of Positioning Failure and its Components," *Proc. 37th Int. Tech. Meeting Satellite Div. Inst. Navig. (ION GNSS+)*, pp. 2228–2249, 2024.
[73] Delft High Performance Computing Centre, Delft Supercomputer (Phase 1), 2022.
[74] I. Papaioannou, S. Geyer, and D. Straub, "Improved cross-entropy based importance sampling with flexible mixture model," *Reliab. Eng. Syst. Saf.*, vol. 191, pp. 1–11, 2019.
[75] F. Uribe et al., "Cross-Entropy-Based Importance Sampling with Failure-Informed Dimension Reduction for Rare Event Simulation," *J. Uncertain. Quantif.*, vol. 9, nb. 2, pp. 818–847, 2021.

Sebastian Ciuban received the M.Sc. in Aerospace Systems: Navigation and Telecommunications from École Nationale de l'Aviation Civile (ÉNAC), Toulouse, France, in 2017. He is currently pursuing the Ph.D. degree in GNSS safe-positioning for automated and autonomous vehicles with Delft University of Technology, Delft, The Netherlands. After his M.Sc. degree, he joined the European Space Research and Technology Centre (ESTEC) as a Young Graduate Trainee (YGT) with the Directorate of Navigation. From 2019 to 2021, he was a GNSS Engineer with CGI Nederland B.V. His research interests include the interplay between parameter estimation and statistical hypothesis testing, numerical integration methods, and development of algorithms for safe positioning and navigation.

Peter J.G. Teunissen is Professor of Geodesy and Satellite Navigation at Delft University of Technology, the Netherlands, and member of the Royal Netherlands Academy of Arts and Sciences. His past academic positions include Head of the Delft Earth Observation Institute, Science Director of the Australian Centre for Spatial Information and Federation Fellow of the Australian Research Council. He has been research-active in various fields of Earth Observation, with current research focused on the development of theory, models, and algorithms for high-accuracy applications of satellite navigation and remote sensing systems.

Christian C.J.M. Tiberius received the Ph.D. degree on the subject of recursive data processing for kinematic GPS surveying from the Delft University of Technology, Delft, The Netherlands, in 1998. He is currently an Associate Professor at the Geoscience and Remote Sensing (GRS) Department, Delft University of Technology. His research interests include navigation, with GNSS and terrestrial radio positioning, primarily for automotive applications.